# ADVANCED MIXED MATRIX MEMBRANES FOR BIOFUEL RELATED SEPARATIONS

An Undergraduate Thesis
Presented to
The Academic Faculty

By

Michelle E. Dose

In Partial Fulfillment of the Requirements for the
Undergraduate Research Opportunities Program in the
School of Chemical and Biomolecular Engineering

Georgia Institute of Technology
May 2013

# ADVANCED MIXED MATRIX MEMBRANES FOR BIOFUEL RELATED SEPARATIONS

Approved by:

Dr. William J. Koros, Advisor
School of Chemical and Biomolecular Engineering
*Georgia Institute of Technology*

Dr. Ronald R. Chance
School of Chemical and Biomolecular Engineering
*Georgia Institute of Technology*

Dr. Cliff Henderson
School of Chemical and Biomolecular Engineering
*Georgia Institute of Technology*

Date Approved: 1 May 2013

# TABLE OF CONTENTS

# SUMMARY

Algae-based biofuels are a promising approach for producing fuel grade ethanol at industrially relevant scales. To achieve this goal, algae processes require large amounts of $CO_2$ to operate efficiently — this $CO_2$ ideally being delivered from large antropogenic point sources. Furthermore, most algae processes encumber a large energy penalty due to the need fore purification of ethanol from dilute ethanol streams. High performance mixed matrix membranes (MMM) can be used to reduce the cost of separations required to maintain desirable $CO_2$ concentrations in algae photobioreactors and to produce a pure ethanol product. For the latter, to achieve the desired ethanol purity, hydrophobic molecular sieves with high ethanol/water selectivity, such as fluoride mediated silicalite-1 (a highly hydrophobic zeolite) and ZIF-71 (a hydrophobic zeolitic imidazolate framework), are required. Initial vapor sorption results show silicalite-1 ($F^-$) has an ethanol uptake of 2.27 mmol/g with a minimal water uptake of only 0.26 mmol/g at unit activity, yielding an ethanol/water sorption selectivity of 53 for feeds of 1-5 wt% ethanol. Vapor isotherms for ZIF-71 show an ethanol uptake of 3.0 mmol/g with a water uptake of 0.1 mmol/g at unit activity, giving a sorption selectivity of 54 for feeds of 2 wt% ethanol. These molecular sieves were incorporated into poly(dimethyl siloxane) (PDMS) to form MMMs for ethanol removal from water via pervaporation. To supply the photobioreactors with sufficiently pure $CO_2$, various ZIFs were embedded in highly permeable polyimide membranes to form MMMs for $CO_2$ capture from dilute point sources. When compared to pure polymer films, 20 wt% loading of ZIF-8 in 6FDA-DAM-DABA(4:1) led to a 147% increase in $CO_2$ permeability and only a 5% decrease in ideal $CO_2/N_2$ selectivity. These promising results predict hollow fiber performance within commercially attractive region for $CO_2$ from dilute point sources.

# CHAPTER 1

# INRODUCTION

## *1.1. Membrane Separations*

In recent years, the drive to achieve more efficient and environmentally friendly separation techniques has resulted in the rapid development of membrane processes. Many different industrial membrane separation techniques have emerged over the past few decades and new processes are constantly being developed. Membranes and membranes processes cover a broad range of applications, including the production of potable water from the sea, the treatment of industrial effluents, removal of toxins from the blood stream, and to fractionate, concentrate, and purify solutions in the pharmaceutical, chemical, and biofuel industries [1]. Advances made in membrane materials, membrane structure, and large scale production methods have made some membrane separation processes superior to many conventional mass separation methods. Compared to their counterparts, membranes can allow for faster processing, rather simple continuous operation, and can be "tailor-made" so their properties can be adjusted to a specific separation.

Membrane-based separations involve the use of a membrane as a thin barrier to separate a mixture. During the separation process, a driving force, such as a concentration or pressure differential, is applied to allow preferential transport of one or more feed components across the membrane. Two common characteristics used to describe the performance of membranes are the permeability (the ability of permeates to pass through a membrane, sometimes referred to as productivity) and selectivity (the ratio of permeability of the more permeable component to that

of the less permeable, sometimes referred to as efficiency). A higher permeability reduces the area required for a separation, while a high selectivity will result in a higher purity product. For a membrane to be useful for separation or purification processes, it must exhibit the desired permeability and selectivity, as well as possess the required mechanical stability, a resistance to fouling, and low cost [2].

### *1.2. Polymeric Membranes*

Polymers provide a range of characteristics desirable for membrane separations, including ease of processability, low cost, and good mechanical stability, making polymeric membranes one of the most common types of membranes. The mechanism of permeation in polymeric films can be described by the sorption-diffusion model, in which a penetrant is sorbed into the dense film from a higher activity upstream, diffuses through the film driven by a chemical potential gradient, and is then desorbed on the lower activity downstream [3]. In this model, permeability of a molecule, $P_i$, can be expressed as the product of diffusivity, $D_i$, and sorption, $S_i$, of the molecule in the polymer.

$$P_i = D_i * S_i \tag{1.1}$$

Molecules can have high permeability coefficients due to high sorption coefficients, high diffusion coefficients, or a combination of the two. Because selectivity can be described as the ratio of permeabilities, Equation 1 can be rewritten such that the efficiency of a membrane can be given as a product of diffusive and sorptive selectivities, as shown in Equation 2.

$$\alpha_{ab} = \frac{P_a}{P_b} = \frac{D_a}{D_b} \cdot \frac{S_a}{S_b} \tag{1.2}$$

This relationship indicates that selectivity can be improved by enhancing either the solubility or the diffusivity. This noted, polymers that exhibit high selectivity tend to be less permeable and vice versa [4]. This general trade-off that exists between selectivity and permeability was noticed

by Robeson and has brought about so-called "polymer upper-bound" limits for many common molecular pairs [5, 6]. A substantial research effort has been directed at overcoming the limit imposed by the upper bound and to achieve membranes with performances in the commercially attractive region highlighted in Figure 1.1.

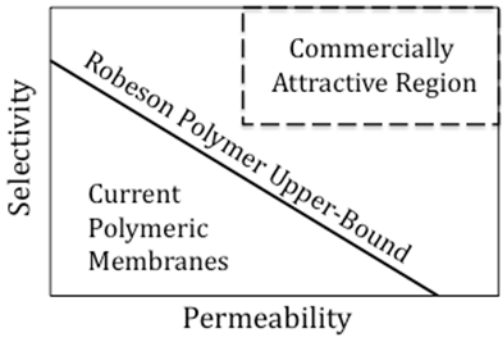


**Figure 1.1:** Generalized trade-off plot showing the limitations of current polymeric membranes and the commercially attractive region.

*1.3. Inorganic Membranes*

Inorganic membranes, such as those composed purely of molecular sieving zeolites, alumina, carbon, or silica (among many others), typically have higher thermal and chemical stabilities, making them useful under conditions which polymeric membranes will fall short. Additionally, inorganic membranes can greatly outperform polymeric membranes due to the separation mechanism being dominated by molecular sieving [7]. Although this allows for very high selectivities and permeabilities, inorganic membranes tend to have poor processability and are just now finding applications in some gas phase separations.

*1.4. Concept of Mixed Matrix Membranes*

In attempts to overcome the limits imposed by polymeric and inorganic membranes, new types of membranes, mixed matrix membranes, have recently been introduced. These so called mixed matrix membranes (MMM) are comprised of a continuous polymer phase, either glassy or

rubbery, with uniformly distributed fillers that will ideally improve membrane performance beyond the trade-off curve. The presence of the selective filler creates a highly impaired path for the un-favored molecule, decreasing the flux of that component (see Figure 1.2). The permeability of the desired component is usually enhanced, or at least un-impaired, by the presence of the fillers, and thus the membrane's overall selectivity is generally improved.

Material selection for both polymer and filler is a key aspect in the development of successful mixed matrix membranes. While there are three main types of MMMs, solid-polymer, liquid-polymer, and solid-liquid-polymer, the first of the three will henceforth be the topic of primary focus.

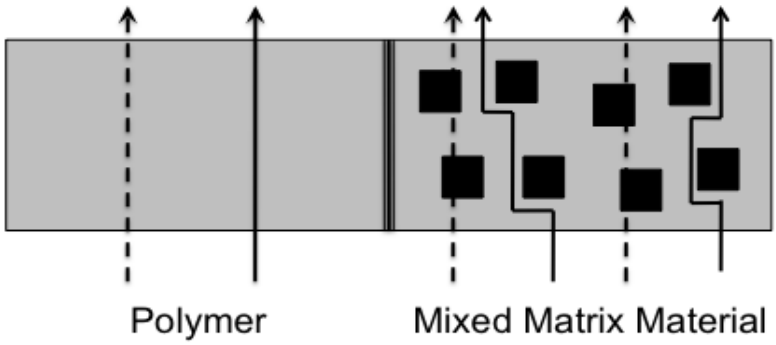


**Figure 1.2:** Comparative transport pathways of molecular species in polymer and mixed matrix materials. From [8].

**REFERENCES**


1. MC Porter. *Handbook of industrial membrane technology*. 1990.
2. C Liu, et al. Recent Progress in Mixed-Matrix Membranes, *Advanced Membrane Technology and Applications*. Wiley: Hoboken, NJ. 2008. p 787 – 819.
3. P Pandy, R Chauhan. Membranes for gas separation. *Progress in Polymer Science,* 2001. 26(6). p 853 – 893.
4. SA Stern. Polymers for gas separations: the next decade. *Journal of Membrane Science*, 1994. 94(1). p 1 – 65.
5. LM Robeson. Correlation of separation factors verses permeability for polymeric membranes. *Journal of Membrane Science*, 1991. 62(2). p 165 – 185.
6. LM Robeson. The upper bound revisited. *Journal of Membrane Science*, 2008. 320(1). p 390 – 400.
7. M Mottern, et al. Microstructural Optimization of Thin Supported Inorganic Membranes for Gas and Water Purification. *Advanced Membrane Technology and Applications*. Wiley: Hoboken, NJ. 2008. p 899 – 928.
8. JR Johnson. Scalable Techniques for the Formation of Polymer-Nanoplatelet Hybrid Membranes and Characterization Thereof. *School of Chemical and Biomolecular Engineering*

# CHAPTER 2

# SOLID-POLYMER MIXED MATRIX MEMBRANES

## 2.1. Development of Solid-Polymer Mixed Matrix Membranes

While mixed matrix membranes offer the ease of processing of polymers and the high selectivity of molecular sieving materials, this new technology comes with a number of challenges currently hindering development. Such roadblocks include selection of materials with similar transport properties, homogenous dispersion of the filler in the polymer matrix, and polymer-filler interfacial compatibility.

Ideally, a mixed matrix membrane would combine a polymer with a filler that has the highest selectivity and permeability available. Unfortunately, this method would only be applicable if the filler was present in high concentrations, which is very difficult to process. Therefore, it is necessary to select polymers and dispersed phases that possess compatible transport properties. Once the transport properties of the polymer and filler are known, there are several models that can be used to predict the productivity and efficiency of theoretical mixed matrix membranes [1, 2]. These calculations allow one to estimate the necessary filler loading to achieve the desired separation properties.

Once the materials have been selected, the filler must be effectively dispersed. This can typically be accomplished by using some form of mechanical energy input (e.g. blending, vortex mixing, sonication) to disperse the nano-sized particles and then stabilizing the suspension in a viscous polymer solution [3]. It is important that the dispersed phase remain stable during the membrane formation process, otherwise new issues, such as particle settling or agglomeration, could arise and influence the effectiveness of the membrane.

The transport properties of hybrid membranes are strongly dependent on the nanoscale morphology, particularly at the interfacial region between the polymer matrix and the filler surface. Non-ideal polymer-filler interaction in this region is the primary source of defects in hybrid membranes [4-7]. The type of morphology that forms at the interface directly impacts the membrane's separation properties. Avoiding these interfacial defects during membrane formation has slightly hindered the advancement of MMM, especially when high filler loading is desired. Many methods, such as sieve surface modifications, chemical functionalization of the sieve surface, and polymer-sieve grafting, have been used to improve the interface morphology. The necessary modifications, as well as the membrane processing techniques, are often dependent on the filler/polymer combination.

As noted earlier, solid-polymer mixed matrix membranes are one of the most common types of MMM. The dispersed phase is often comprised of microporous molecular sieves (i.e. zeolites, carbon molecular sieves, metal organic frameworks) mesoporous molecular sieves, metal oxides, non-porous silica particles, and carbon nanotubes [4, 8-13]. Microporous molecular sieves possess defined pore structures that make them ideal for the separations. Specifically selected sieves for the desired separations will be discussed in further detail in the following sections.

### *2.2. Applications of Mixed Matrix Membranes in the Biofuels Industry*

#### *2.2.1. Separations around bioreactors*

Algae-based biofuels are a promising approach for generating fuel additives at industrially relevant scales. In a recently developed Direct-to-Ethanol® process, cyanobacteria are housed in a specialized photobioreactor containing seawater and supplied with nutrients and

carbon dioxide. On exposure to sunlight, the algae undergo photosynthesis and produce internal sugars that are converted to ethanol and secreted through the cell wall into the culture medium. Along with the secreted ethanol, photobioreactor water evaporates into the bioreactor headspace where it condenses on the photobioreactor walls and is collected [14, 15]. For this to be achieved on the industrial scale, large amounts of sufficiently pure $CO_2$ must be fed to the bioreactors to operate efficiently—ideally this $CO_2$ is delivered from large point sources. Furthermore, the dilute ethanol-water mixture (about 1 wt% ethanol) collected from the bioreactors must be concentrated to greater than 99.5 wt% ethanol in order to meet standards for fuel grade ethanol (Figure 2.1). As with most algae processes, the separations centered on these photobioreactors can encumber a large energy penalty due to purification of the dilute ethanol-water stream and separation of $CO_2$ from other components (particularly $N_2$) found in flue gas streams or other large point sources. High performance mixed matrix membranes can potentially be used to reduce the cost of separations required to maintain the bioreactors and produce a pure ethanol product.

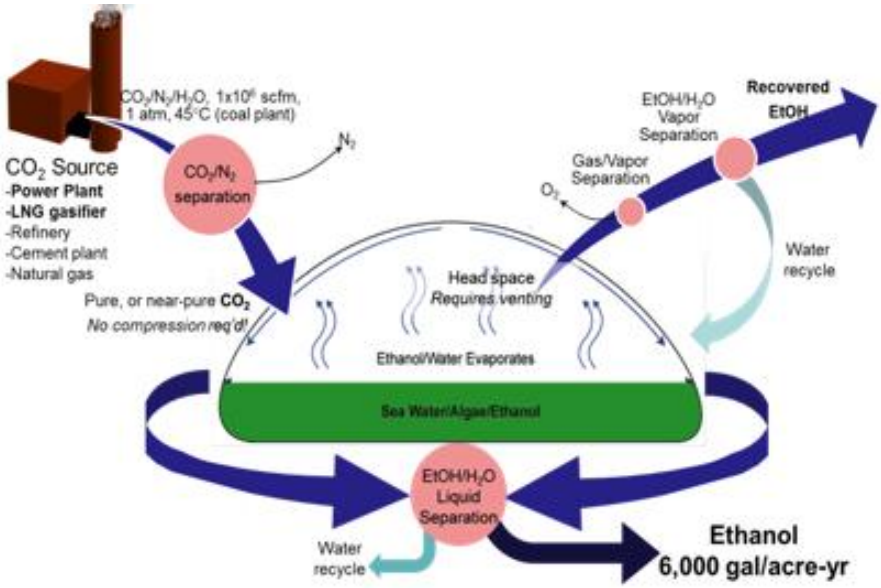


**Figure 2.1:** Photobioreactor showing necessary separations centered around Algenol's Direct-to-Ethanol® process.

*2.2.2 Mixed Matrix Membranes for $CO_2/N_2$ Separations*

Over the past several decades, the rise in atmospheric $CO_2$ has been of great concern. Many initiatives, such as the U.S. Global Climate Change Initiatives (GCCI), have been implemented with hopes of slowing growth in U.S. emissions of carbon dioxide. With combustion of fossil fuels generating the largest portion of greenhouse gases, it is desired to capture and purify this $CO_2$ for use in maintaining algae-based biofuel systems. Currently, alkaline sorbents, scrubbing solutions, and cryogenic distillation are used to separate carbon dioxide from various gas mixtures. However, these methods have critical drawbacks due to the large volume and low pressure of flue gas. Development of membranes for selective removal of $CO_2$ from these streams would be of great economic value.

Two types of polymers are widely used to form membranes for commercial gas separations. Glassy polymers are rigid and operate below their glass transition temperatures, compared to rubbery polymers, which are soft and flexible and operate above their glass transition temperatures. In general, rubbery polymers exhibit high permeability with low selectivities; whereas glassy polymers tend to have low permeability and high selectivities. Due to their high selectivity and good mechanical properties, glassy polymeric membranes dominate industrial membrane separations.

To overcome the low permeation rates of adequately selective polymers, asymmetric membranes are often used. The membranes consist of a thin, dense, selective layer supported by a porous, non-selective layer of the same material [16]. Such membranes can be spun into high surface area per unit volume hollow fiber membranes with selective layers as thin as a few hundred nanometers [16, 17]. Membranes spun with thin selective layers often have pinhole defects, which allow feed components to bypass the selective layer, greatly reducing the overall

membrane selectivity. This problem can be overcome by coating the hollow fibers with a thin, fast permeating, non-selective polymer, such as silicone rubber, to essentially plug the holes without reducing the bulk polymer permeability [18]. These hollow fibers can be packed into modules that can contain thousands of square feet of membrane surface area per cubic foot of module volume and can be connected in series and/or in parallel to achieve the desired productivity and product purity [19].

To minimize the energy necessary to maintain the pressure ratio (the driving force for separation) across the membrane, Favre determined the optimum membrane/pump configuration to be "as-received" flue gas on the feed side with a vacuum pump on the down stream side [20]. In this configuration, flue gas is swept across the shell side of the fibers (to minimize compression costs), while vacuum is pulled on the bore side to supply the necessary pressure ratio across the membrane. Additionally, this configuration bypasses the need to compress the excess nitrogen present in the flue gas by only doing the work on the product, thereby minimizing the membrane process energy requirements.

There are not many rubbery polymers, other than PDMS and polyethyleneoxide, that are used in gas separations. On the other hand, many glassy polymers such as polyacetylenes, poly[1-(trimethylsilyl)-1propyne] (PTMSP), polyimides, polyamides, polyarylates, polycarbonates, polysulfones, cellulose acetate, poly(phenylene oxide), and cardo-type polymers are often studied polymeric materials for gas separations [21]. Polyimides are one of the most investigated classes of polymers for membranes separation. These polymers tend to exhibit higher gas selectivity, as well as higher gas permeability compared to many other glassy polymers [22]. In particular, polymers based on fluorinated dianhydride (5,5'-[1,1,1-trifluoro- 1-(trifluoro- methyl) ethylidiene] bis-l,3-isobenzofurandione (6FDA) have exhibited high

permeability with a strong affinity to carbon dioxide when functionalized with various groups, making it a particular polymer of interest for flue gas separations.

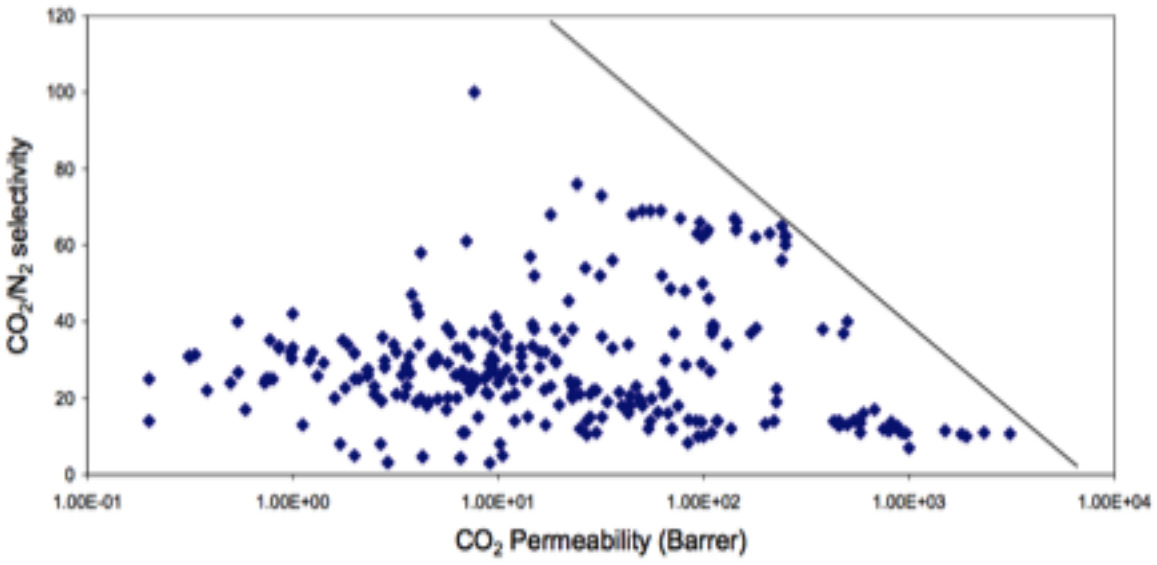


**Figure 2.2:** Summary of literature data for $CO_2/N_2$ selectivity vs. $CO_2$ permeability for polymeric membranes showing the Robeson upper bound for this gas pair. From:[22].

To extend the performance of the polymer beyond the upper bound, mixed matrix membranes will be formed using the functionalized form of 6FDA. To improve the selectivity of the membranes, it is desired to enhance the diffusivity selectivity by embedding molecular sieves with pore sizes between that of the kinetic diameter of $CO_2$ and $N_2$ (3.3 Å and 3.8 Å, respectively), so that $CO_2$ can pass through unimpeded while $N_2$ is rejected. Similar to the work done by others using different polymers [23], asymmetric hollow fiber membrane will be formed using the 6FDA polymer and ZIF-8 (pore size of 3.4 Å). Other fillers with appropriate pore size for separation of $CO_2/N_2$ include ZIF-7 (2.9 Å) and various zeolites are considered. Such fillers can be used to improve both the productivity and efficiency of 6FDA polymers as well as silicone rubber [24].

*2.2.3. Ethanol Selective Mixed Matrix Membranes for Pervaporation*

The conventional method used for the separation of dilute ethanol-water mixtures is a standard distillation process followed by molecular sieve adsorption to further purify the ethanol to fuel grade levels. Even though this method achieves the necessary separation, it is not cost effective due to large amount of energy required to heat and vaporize excess amounts of water. In an effort to reduce the energy required for the separation of ethanol-water mixtures, extensive research has been invested in developing ethanol-selective membranes for use in pervaporation. Pervaporation is a process in which a liquid feed stream composed of two miscible components is placed in contact with one side of a selective membrane while vacuum, or a gas purge, is applied to the other side. The components of the liquid stream sorb into the membrane, permeate through the membrane, and evaporate into the vapor phase (Figure 2.3). The resulting vapor, referred to as the permeate, is then condensed. As shown in Equation 2, the effectiveness of the membrane is determined by the species in the feed mixture having different affinities for the membrane and different diffusion rates through the membrane. As it is desirable to have ethanol selective membranes, the diffusivity selectivity has little positive influence on the efficiency of the membrane and separation is predominantly controlled by the sorption selectivity of the materials.

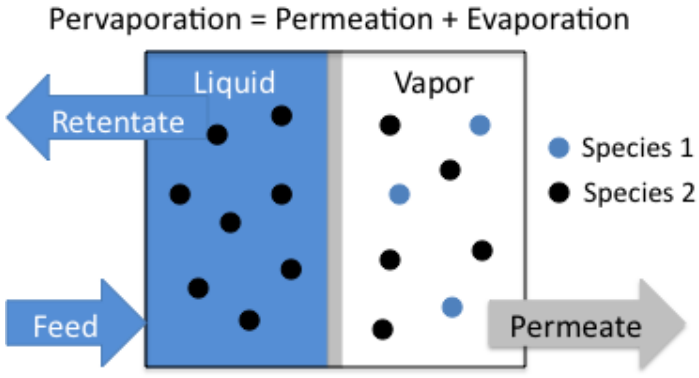


**Figure 2.3:** Schematic diagram of pervaporation process[25]

In order to compare the efficiency of an ethanol recovery technology, the energy required to recover a unit of ethanol must be determined. For pervaporation, the energy expended to recover the ethanol can be estimated from the heats of evaporation of ethanol and water (838 kJ $kg^{-1}$ and 2260 kJ $kg^{-1}$, respectively), the ethanol-water separation factor (βew), the ethanol concentration in the feed, and the desired degree of recovery of ethanol [25]. The separation factor is the parameter traditionally used to describe the separation capability of the membrane and is defined as the ratio of the ratio of permeate compositions, ($C_e^V/C_w^V$) to the ratio to the ratio of feed compositions ($C_e^L/C_w^L$), viz.,

$$\beta_{ew} = \frac{C_e^V/C_w^V}{C_e^L/C_w^L} \tag{2.1}$$

In an extensive analysis, Vane was able to determine energy requirement estimates for 95% ethanol recovery by pervaporation for membranes with various separation factors [25]. For comparison, energy requirements for large-scale, heat-integrated distillation systems were included. As seen in Figure 2.4, membranes with separation factors greater than 20 are required to yield the same energy efficiency as distillation.

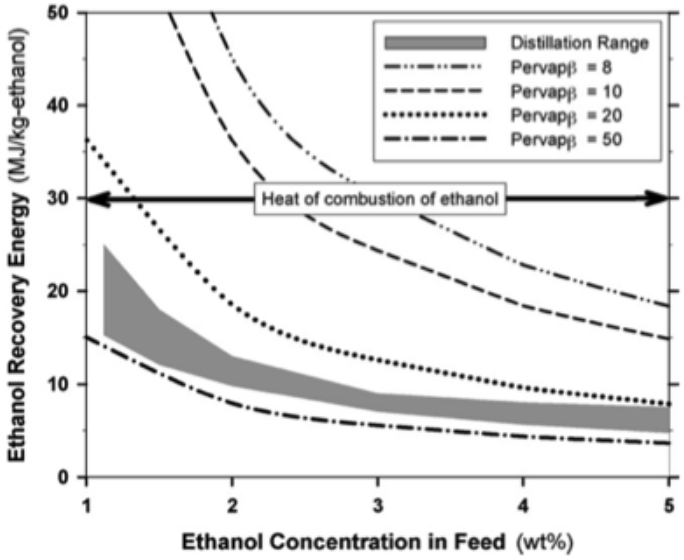


**Figure 2.4:** Energy required to recover ethanol from water as a function of ethanol concentration in the feed stream for distillation systems and pervaporation systems at several ethanol-water separation factors. Ethanol recovery of 95% assumed for pervaporation. From [26].

The standard reference hydrophobic membranes for ethanol removal from water are composed primarily of poly(dimethyl siloxane), commonly referred to as PDMS or silicone rubber. Compared to other hydrophobic ethanol permeable polymers, PDMS has a both a higher flux and higher ethanol-water selectivity. Reported separation factors for pure silicone rubber membranes average between 7-8, values well below the target of $\beta_{ew} > 20$ for the previously mentioned scenario [26]. To improve the effectiveness of PDMS, mixed matrix membranes are typically formed using hydrophobic MFI-type zeolites, particularly silicalite-1, as the dispersed phase. In the data summarized by Vane (Figure 2.5), these membranes have separation factors ranging from 7.5 (for 10 wt% zeolite loading) to 59 (for 75 wt% loading) [26]. While some of these membranes meet the desired specifications, there still stands much room for improvement. In particular, membranes containing 50 wt% of various ZSM-5 zeolites (an aluminosilicate form

of MFI) have reported βew ranging from 5 to 29.3 and tend to exhibit a decrease in selectivity with prolonged testing [12, 26- 32]. Recently, this general degradation in performance has been attributed to water interacting with internal sites in the zeolite. These internal sites could be associated with general defects, particularly lattice defects and surface silanols, in the zeolite structure [29, 33]. To reduce the effects of silanol defects, the alteration of the surface chemistry of zeolites through treatment with organosilanes and alcohols have been reported in the literature [29, 34-36]. When the defective zeolites were quenched in ethanol and n-butanol prior to being dispersed in PDMS, the membranes exhibited only a slight downward trend in ethanol-water separation factor with prolonged testing. Such results are promising for the advancement in silicalite-PDMS mixed matrix membranes, making them more likely prospect for use industrial applications.

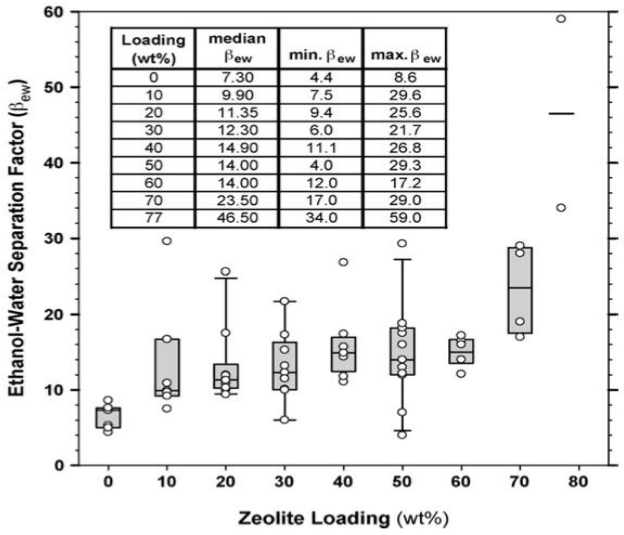


**Figure 2.5:** Ethanol-water separation factors reported in the literature for high silica ZSM-5 zeolite-silicone rubber mixed matrix membranes. Open circles represent all data points used in analysis. Boxes: lower bound=25$^{th}$ percentile, upper bound=75$^{th}$ percentile, inter line=median, whiskers represent 10$^{th}$/90$^{th}$ percentiles when 9 or more points were available. From [26].

Although the alteration of the surface chemistry of the various silicalites proved effective at stabilizing the ethanol-water selectivity over extended time, the hydrophobicity of the silicalite is still greatly affected by the presence of lattice defects and silanols within the inner workings of the zeolite. If such defects could be minimized, or even eliminated, the hydrophobicity of the zeolite could be increased and a membrane with higher efficiency could be produced. A specialized hydrophobic MFI-type zeolite has recently been developed that exhibits an ethanol-water sorption selectivity greater than 90 for feeds of 1-5 wt% ethanol.

Other hydrophobic materials could be used in place of zeolites. One such material that has yet to be used in mixed matrix membranes is zeolitic imidazolate framework 71 (ZIF-71). ZIFs are a class of metal organic framework (MOF) that are formed via coordination between metal centers and organic imidazolate linkers [37].

### *2.3 Objectives*

The purpose of this study is to develop highly selective mixed matrix membranes for use in biofuel related separations. In particular, ethanol-selective membranes will be developed for purification of dilute ethanol-water mixtures recovered from algae bioreactors. $CO_2$-selective membranes will be developed for the separation of $CO_2$ from $N_2$ rich flue gas streams. In order to achieve this, the following objectives are proposed:

#### *2.3.1. Objective 1: Select and characterize the appropriate sieve for each separation*

The clear first step in the formation of mixed matrix membranes is selecting the appropriate molecular sieve to be dispersed in a polymer matrix. For ethanol-water separations, the objective is to find fillers that have relatively high ethanol uptake and a low water uptake to

enhance the sorption selectivity. Three fillers were initially considered. The first choice was silicalite-1 synthesized via an alkaline route, referred to as silicalite-1 ($OH^-$), the standard filler used in ethanol-selective membranes. This material is known to have decent ethanol-water sorption selectivity and was chosen as a reference for other fillers. The second choice was ZIF-71, a type of zeolitic imidazolate framework. This sorbent offers an advantage in that it is predicted to be extremely hydrophobic, having an estimated water uptake of only 0.002 mmol/g at near unit activity compared 1.99 mmol/g for silicalite-1 ($OH^-$) [38]. Finally, the third filler choice for this separation was silicalite-1 synthesized via a fluoride mediated route, silicalite-1 ($F^-$). This filler is believed to have a similar ethanol uptake as silicalite-1 ($OH^-$), but have a much lower water uptake and thus a higher ethanol-water sorption selectivity. In order to select the ideal filler, several characterization techniques were employed, the results of which will be discussed in this work.

For $CO_2/N_2$ separations, it is desired to have fillers that exhibit a high diffusive selectivity for $CO_2$ and $N_2$. Two molecular sieves that have been considered are ZIF-7, with a flexible pore size of 0.29 nm, and ZIF-8, with a flexible pore size of 0.34 nm.

*2.3.2. Objective 2: Select and characterize the appropriate polymer matrix*

In order for the mixed matrix membranes to be successful, appropriate polymers must be selected to support the dispersed phase. The goal of polymer selection is to find a polymer that exhibits good mechanical and thermal stability, as well as good compatibility with the filler as to achieve the ideal interface. Polymers with properties near the upper bound are desired to serve as the polymer matrix. Unfortunately, polymers for ethanol-water separations are few and far between, so the commonly used poly(dimethyl siloxane) (PDMS) will serve as a starting point.

As mentioned previously, many polymers have been investigated for $CO_2/N_2$ separations, especially polyimides. In particular, polymers based on fluorinated dianhydride (5,5'-[1,1,1-trifluoro- 1-(trifluoro- methyl) ethylidiene] bis-l,3-isobenzofurandione (6FDA) have been shown to exhibit properties close to the upper bound for this gas pair. As previous work has shown, 6FDA-DAM constituents tend to promote high $CO_2$ permeability, but low $CO_2/N_2$ selectivity while 6FDA-DABA constituents promote high selectivity with low permeability [39, 40]. 6FDA-DAM-DABA(4:1) was chosen to serve as the middle ground of the previously studied co-polymers using.

*2.3.3. Objective 3: Form defect-free mixed matrix membranes*

After appropriate filler and polymer have been chosen, the next step is to form defect-free mixed matrix membranes. This step is especially difficult due the necessity of homogenously dispersing the filler as well as obtaining an ideal interface between the polymer and filler. As a proof of concept, dense flat mixed matrix membranes were initially formed. Parameters such as solvent choice, casting dope composition and preparation, filler loading, and casting technique and environment were adjusted in order to achieve the best results. Scanning electron microscopy (SEM) was used to confirm proper filler dispersion and polymer adhesion.

To arrive at industrially relevant $CO_2$ fluxes, it is desired to form hollow fiber mixed matrix membranes using the 6FDA-based polymers. To achieve this goal, a proper spin dope is required with polymer/solvent/non-solvent/filler compositions being carefully optimized. Once a proper spin dope is created, spinning conditions must be optimized with relation to the dope composition to produce fibers with a thin, defect-free skin layer and a highly porous substructure. These properties can be controlled by 1) adjusting the air gap between the spinneret

and the quench bath as to control the skin thickness, 2) adjusting the flow rate of the dope and bore fluid to control the shear rate of the spinning solution, 3) adjusting the composition of the bore fluid to control phase separation on the interior of the fiber, 4) adjusting the operating temperatures as to control the rate of phase separation and dope viscosity, and 5) adjusting the take-up rate of the fiber so as to change the time spent in the coagulation bath. As the 6FDA-polymers have not been studied in depth, fibers were initially spun as a neat polymer to prove fibers with the desired characteristics could be achieved. After good fibers have been achieved, mixed matrix hollow fiber membranes will be prepared. To confirm proper filler dispersion and fiber dimensions, SEM will be used. Pure gas permeation experiments will be used to determine the porosity of the substructure as well as to measure the extent of defects in the skin layer.

*2.3.4. Objective 4: Test and analyze performance of membranes*

The final phase of the research will involve observing the performance of the mixed matrix membranes. The CO2-selective membranes will be tested under pure gas conditions using a combination of constant pressure and constant volume gas permeation systems. To observe the membranes performance under mixed gas conditions, a slightly more complicated mixed gas permeation system will be used so the permeate can be fed to a calibrated gas chromatograph for compositional analysis.

To test the performance of ethanol-selective membranes, a bench scale pervaporation system was built. This system will require the design of a stirred pervaporation cell to prevent concentration polarization near the membrane and will include a heated upstream and hot plate to control the operation, a nitrogen cold trap with ground glass joints for sample collection, and a vacuum pump to pull vacuum on the downstream. After the sample is collected, its composition will be analyzed via refractometry and calculations can be done to determine the membrane's overall performance.

**REFERENCES**


1. EE Gonzo, ML Parentis, and JC Gottifredi. Estimating models for predicting effective permeability of mixed matrix membranes. *Journal of Membrane Science*, 2006. 277(1). p 46 – 54.
2. R Pal. Permeation models for mixed matrix membranes. *Journal of colloid and interface science*, 2008. 317(1). p 191 – 198.
3. RD Nelson. *Dispersing powders in liquids*. Ensevier: Amsterdam. 1988.
4. C Liu, et al. Recent Progress in Mixed-Matrix Membranes, *Advanced Membrane Technology and Applications*. Wiley: Hoboken, NJ. 2008. p 787 – 819.
5. R Mahajan, et al. Challenges in forming successful mixed matrix membranes with rigid polymeric materials. *Journal of Applied Polymer Science*, 2002. 86(4). p 881 – 890.
6. TT Moore, et al. Hybrid membrane materials comprising organic polymers with rigid dispersed phases. *AIChE Journal*, 2004. 50(2). p 311 – 321.
7. TT Moore and WJ Koros, Non-ideal effects in organic-inorganic materials for gas separation membranes. *Journal of Molecular Structure*, 2005. 739(1). p 87 – 98.
8. P Pandy, R Chauhan. Membranes for gas separation. *Progress in Polymer Science,* 2001. 26(6). p 853 – 893.
9. JM Duval, et al. Adsorbent filled membranes for gas separations. *Journal of Membrane Science*, 1993. 80(1). p 189 – 198.
10. RT Adams, et al. $CO_2$-$CH_4$ Permeation in High Zeolite 4A Loading Mixed Matrix Membranes. *Journal of Membrane Science*, 2010.
11. KS Park, et al. Exceptional chemical and thermal stability of zeolitic imidazolate frameworks. *Proceedings of the National Academy of Sciences*, 2006. 103(27). p 10186.
12. G Clarizia, C Algieri, and E Drioli. Filler-polymer combination: a route to modify gas transport properties of a polymeric membrane. *Polymer*, 2004. 45(16). p 5671 – 5681.
13. P Goh, et al. Recent advances of inorganic fillers in mixed matrix membranes for gas separations. *Separation and Purification Technology*, 2011.
14. RP Woods, et al. Closed photobioreactor system for continued daily in situ production, separation, collection, and removal of ethanol from genetically enhanced photosynthetic organisms. *Algenol Biofuels*, 2010.

15. D Luo, et al. Life Cycle Energy and Greenhouse Gas Emission for an Ethanol Production Process Based on Blue-Green Algae. *Environmental Science and Technology*, 2010. 44(22). p 8670 – 8677.
16. H Lonsdale. The growth of membrane technology. *Journal of Membrane Science*, 1982. 10(2-3). p 81 – 181.
17. JMS Henis and MK Tripodi. *Multicomponent membranes for gas separations*, 1980.
18. JMS Henis and MK Tripodi. Composite hollow fiber membranes for gas separation: the resistance model approach. *Journal of Membrane Science*, 1981. 8(3). p 233 – 246.
19. WJ Koros and RT Chern. Separation of gaseous mixtures using polymer membranes. *Handbook of Separation Process Technology*. Wiley: New York. 1987. p 862 – 953.
20. E Favre. Carbon dioxide recovery from post-combustion processes: Can gas permeation membranes compete with absorption? *Journal of Membrane Science*, 2007. 291(1). p 50 – 59,
21. D Shekhawat, DR Luebke, and HW Pennline. A review of carbon dioxide selective membranes. *US Department of Energy*, 2003.
22. L Robeson, et al. High performance polymers for membrane separation. *Polymer*, 1994. 35(23). p 4970 – 4978.
23. Y Dai, et al. Ultem/ZIF-8 mixed matrix hollow fiber membranes for $CO_2/N_2$ separations. *Journal of Membrane Science*, 2012.
24. R Banerjee, et al. High-throughput synthesis of zeolitic imidazolate frameworks and application to $CO_2$ capture. *Science*, 2008. 319(5865) p 939 – 943.
25. LM Vane. A review of pervaporation for product recovery from biomass fermentation processes. *Journal of Chemical Technology and Biotechnology*, 2005. 80(6) p 603 – 629.
26. LM Vane, VV Namboodiri, TC Bowen. Hydrophobic zeolite-silicone rubber mixed matrix membranes for ethanol-water separation: Effect of zeolite and silicone component selection on pervaporation performance. *Journal of Membrane Science*, 2008. 308(1-2) p 230 – 241.
27. B Adnadjevic, J Jovanovic, and S Gajinov. Effecto of different physicochemical properties of hybrid zeolites on the pervaporation process of PDMS-membranes. *Journal of Membrane Science*, 1997. 136(1-2) p 173 – 179.

28. SB Tantekin-Ersolmaz, et al. Effecto of zeolite particle size on the performance of polymer-zeolite mixed matrix membranes. *Journal of Membranes Science*, 2000. 175(2) p 285 – 288.

29. LM Vane, VV Namboodiri, and RG Meier. Factors affecting alcohol-water pervaporation performance of hydrophilic zeolite-silicone rubber mixed matrix membranes. *Journal of Membrane Science*, 2010. 364(1-2) p 102 – 110.

30. M Jia, KV Peinemann, and RD Behling. Molecular sieving effect of the zeolite-filled silicone rubber membranes in gas permeation. *Journal of Membrane Science*, 1991. 57(2-3) p 289 – 292.

31. M Jia, KV Peinemann, and RD Behling. Pervaporation and characterization of thin-film zeolite-PDMS composite membranes. *Journal of Membrane Science*, 1992. 73(2-3) p 119 – 128.

32. X Chen, Z Ping, and Y Long. Separation properties of alcohol-water mixture through silicalite-I-filled silicone rubber membranes by pervaperation. *Journal of Applied Polymer Science*, 1998. 67(4) p 629 – 636.

33. M Trzpit, et al. The effect of local defects on water adsorption in silicalite-1 zeolite: a joint experimental and molecular simulation study. *Langmuir*, 2007. 23(20) p 10131 – 10139.

34. CH Cheng, et al. Functionalization of the internal surface of pure-silica MFI zeolite with aliphatic alcohols. *Journal of Physical Chemistry C*, 2008. 112(10) p 3543 – 3551.

35. T Kawai and K Tsutsumi. Reactivity of silanol groups on zeolite surfaces. *Colloid & Polymer Science*, 1998. 276(11) p 992 – 998.

36. T Kawai and K Tsutsumi. A study on the surface silanol groups developed by hydrothermal and acid treatment of faujasite type zeolites. *Journal of Colloid and Interface Science*, 1999. 212(2) p 310 – 316.

37. H Wu, W Zhou, and T Yildirim. Hydrogen storage in a prototypical zeolitic imidazolate framework-8. *Journal of the American Chemcial Society*, 2007. 129(17) p 5314 – 5315.

38. A Nalaparaju, X Zhao, and J Jiang. Molecular Understanding of the Adsorption of Water and Alcohols in Hydrophili and Hydrophobic Zeolitic Metal-Organic Frameworks. *The Journal of Physical Chemistry C*, 2010. 114(26) p 11542 – 11550.

39. JH Kim, WJ Koros, and DR Paul. Effects of $CO_2$ exposure and physical ageing on crosslinking. *Journal of Membrane Science*, 2006. (282) p 32 – 43.

40. W Qiu, CC Chen. L Xu. WJ Koros. Effects of polyimide chemical structure on membrane gas separation performance. *Proceedings of the North American Membrane Society*. Annual Meeting, New Orleans, LA. June 13 2012.

# CHAPTER 3

# HIGH FLUX POLYIMIDE HOLLOW FIBER MEMBRANES FOR $CO_2$ RECOVERY FROM FLUE GAS

## *3.1. Introduction*

While rubbery membranes have received considerable attention for use in post-combustion $CO_2$ capture [1-4], the difficulties associated with mass production of small-footprint, surface area efficient devices hinder their use on the industrial scale. 6FDA-based glassy polymers, on the other hand, have proven to have tunable transport properties and can readily be spun into hollow fiber membranes [5-7]. Due to the large volume of gas necessary to process in post-combustion $CO_2$ capture, high $CO_2$ flux through the membrane with a satisfactory $CO_2/N_2$ selectivity (>~20) is necessary in order to minimize the required membrane area and to meet requirements to capture the advantages of a two-step counter-flow/sweep multistage process [8].

To achieve this goal of a polymer with high flux and moderate selectivity, a 6FDA dianhydride-based copolymer using constituent ratios of DAM and DABA diamines was chosen. As previous work has shown, 6FDA-DAM constituents tend to promote high $CO_2$ permeability, yet low $CO_2/N_2$ selectivity while 6FDA-DABA constituents promote high selectivity with low permeability [9, 10]. To find the middle ground between the previously studied 6FDA-based copolymers, 6FDA-DAM:DABA(4:1) was synthesized and dense films and hollow fiber membranes were formed and characterized.

In an attempt to boost the permeability of 6FDA-DAM:DABA(4:1), a mixed matrix membrane approach was explored. Commercially available zeolitic imidazolate framework (ZIF) "ZIF 8" was used as a permeability-enhancing filler. ZIF 8 has been shown to be (i) highly hydrophobic [11], (ii) highly permeable to $CO_2$ with moderate $CO_2/N_2$ selectivity [12], (iii) and easily dispersed in polymer matrices [12, 13]. While other selectivity enhancing fillers (such as zeolites) exist, there are few that can withstand the high water activities found in combustion flue gas and can be readily incorporated into a polymer matrix without surface enhancement.

The work summarized in the remainder of this chapter has been adapted from the work published in the Journal of Membrane Science [14].

### *3.2. Materials and Methods*

#### *Polymer Synthesis*

6FDA-DAM:DABA(4:1) was synthesized through a one-pot, two-step reaction sequence [CChen2011]. Dried 4,4'-hexafluoroisopropylidene diphthalic anhydride (6FDA) was reacted with dried 2,4,6-trimethyl-1,3-diaminobenzene (DAM) and 3,5-diaminobezoic acid (DABA) under flowing $N_2$ in a 5:4 (6FDA:DAM) and 5:1 (6FDA:DABA) molar ratio in NMP (20wt% solids). The reaction was held between 0°C and 5°C while the diamines were added incrementally over a 2 h period. The slow addition and low temperatures were necessary inorder to form high molecular weight polymer. The reaction was then run for 24 h, during which the temperature was allowed to slowly return to room temperature. The resulting polyamic acid was closed through chemical imidization, whereby beta picoline and acetic anhydride were added and stirred for an additional 24 h under flowing $N_2$ at room temperature. The resulting 6FDA-

DAM:DABA copolymer was then precipitated and washed in methanol, followed by vacuum dring at 210C for 24 h.

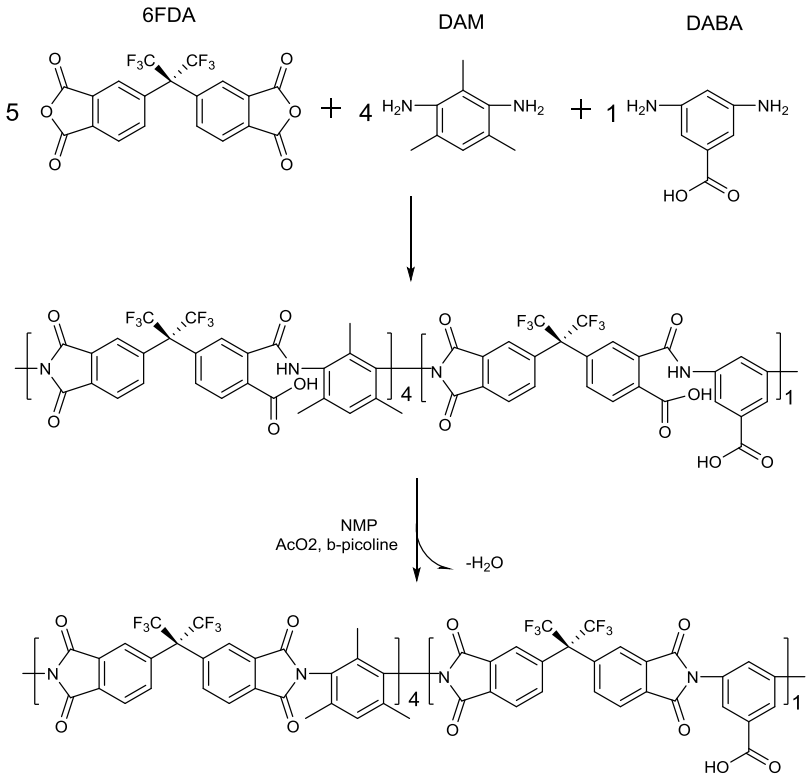


**Figure 3.1.** Synthesis of 6FDA-DAM:DABA(4:1).

*Dense Film Casting*

Dense films of pure 6FDA-DAM:DABA(4:1) were cast from 6FDA:DAM:DABA(4:1)-dichloromethane solutions. The solutions were allowed to mix on a coaxial roller under a heat lamp for 24 h prior to use. Dense films were prepared by pouring a portion of the solution onto an untreated glass plate and casting with a 10 mil casting knife in a $N_2$ filled, dichloromethane saturated glove bag. After allowing the film to stand for 18-24 h in the glove bag, the film was removed from the plate and transferred to a 200°C vacuum oven for 24 h and then allowed to cool naturally to room temperature.

To prepare 20wt% ZIF-8 in 6FDA-DAM:DABA(4:1) mixed matrix membranes, approximately 0.75 g of ZIF-8 (Sigma Aldrich, vacuum dried) was dispersed in 27 g of DCM using three 60 s bursts from a sonication horn (1000W max horn, Dukane, Leesburg, VA) with 90 s of vigorous vortex mixing (Digital Vortex Mixer 120V, Fisher Scientific) between burst. Immediately following the last sonication treatment, 3 g of dried polymer was slowly added, using vigorous vortex mixing after each addition to dissolve the polymer. Sonication of the polymer in the presence of ZIF-8 was avoided as an unknown undesirable reaction between the two components was accelerated, causing the solution to form an gel that was impossible to properly cast. Immediately after all the polymer was dissolved, the ZIF-8/DCM/6FDA-DAM:DABA(4:1) mixture was cast in the same conditions as the pure polymer film. The same drying and annealing procedures were followed. A sample of intentionally gelled ZIF-8/DCM/6FDA-DAM:DABA(4:1) was also prepared for X-ray diffraction analysis.

*Hollow Fiber Spinning*

Using a dry-jet, wet-quench, non-solvent-induced phase separation spinning, 6FDA-DAM:DABA(4:1) hollow fibers were produced. The spinning dopes were prepared based on dopes capable of making defect free skin layers for a similar polymer, 6FDA-DAM:DABA(4:1) [6]. The dope composition and spinning conditions can be found in Table 3.I [7]. The polymer solution was stirred for a week in a sealed container on stirred on a coaxial roller at 45°C until a clear, viscous solution was obtained. After degassing, the dope was loading into a 500 mL ISCO pump (Model 500D, Teledyne ISCO, Inc., Lincoln, NE). The fibers were extruded through a "spinneret" into a 50°C, 2 m transversal length water bath and were taken up at 50 m/min. After removing from the take-up drum, the fibers were soaked in deionized water for 3 days, changing

the water each day. After the water soak, the fibers were solvent exchanged in methanol for 1 hr, changing the methanol every 20 min. After repeating the same process with hexane, the fibers were allowed to air dry for one day, and then placed in a 110C vacuum oven for 1 h.

**Table 3.I.** 6FDA-DAM:DABA(4:1) hollow fiber dope formulation and spinning conditions.

| **Dope Formulation** | | **Spinning Conditions** | |
|---|---|---|---|
| Polymer | 25.0 wt% | Dope extrusion rate | 180 mL $h^{-1}$ |
| NMP | 31.5 wt% | Bore fluid | 60 mL $h^{-1}$, 80/20wt% NMP/$H_2O$ |
| THF | 10.0 wt% | Bath temperature | 50°C |
| $LiNO_3$ | 6.5 wt% | Spinneret temperature | 70°C |
| Ethanol | 27.0 wt% | Air gap | 2-16 cm |
| | | Quench bath | Tap water, 2 m traversal length |
| | | Take-up rate | 50 m $min^{-1}$ |

*Materials Characterization*

Differential scanning calorimetry (DSC, model TA Instruments Q200) was used to measure the glass transition temperatures for neat 6FDA-DAM:DABA(4:1) and its corresponding mixed matrix membrane. Runs were made from 0°C to 420°C at a heating rate of 10°C/min, using the second sweep to determine the $T_g$. The degradation temperatures of the membranes were determined using termogravimetric analysis (TGA, Netzch STA 409 PC TGA Burlington, MA). The samples were heated to 600°C under a nitrogen purge at a ramp rate of 10C/min. Powder X-ray diffraction (XRD) was performed at room temperature on an X'Pert Pro PANalytical X-ray Diffractometer using Cu-Kα radiation. Measurements were carried out from 5-40° 2θ, using an X'celerator detector with low-background sample holders. Attenuated total reflectance spectroscopy (ATR) was performed using a Bruker Vertex 80v FTIR spectrometer coupled to a Hyperion 2000 IR microscope containing a 20x magnification ATR objective with a Germanium crystal.

*Permeation*

Building on the sorption diffusion model previously discussed (Equation 3.1), permeability can further difined as the flux of component *i* normalized by the pressure applied across the membrane, $\Delta p$, and the film thickness.

$$P_i = \frac{(flux)_i \ell}{\Delta p_i} \tag{3.1}$$

In cases where the skin thickness is difficult to determine, like in asymmetric membranes, the "permeance" can be defined as the flux normalized by the partial pressure difference, given by:

$$\left(\frac{P}{\ell}\right)_i = \frac{(flux)_i}{\Delta p_i} \tag{3.2}$$

Permeation though a membrane occurs via an activated process which exhibits an apparent Arrhenius dependence on temperature,

$$P_i = P_{i,0} \exp\left(-\frac{E_{P,i}}{RT}\right) \tag{3.3}$$

where $P_{i,0}$ is the exponential pre-factor and $E_P$ is the activation energy of permeation. Likewise, temperature dependence of diffusion of gas though a film can be defined as

$$D_i = D_{i,0} \exp\left(-\frac{E_{D,i}}{RT}\right) \tag{3.4}$$

where $D_{i,0}$ is the pre-factor and $E_D$ is the activation energy of diffusion.

Permeation tests on the dense 6FDA-DAM:DABA(4:1) were performed using an isochoric system [15,16], where the intrinsic permeability of the polymer can be calculated using measurements of the film's thickness, permeable surface area, feed pressure, and the pressure rise in the downstream of the system (which is proportional to the molar flow rate through the film). $N_2$ was tested first, followed by $CO_2$, and then $N_2$ was retested to confirm the polymer did not undergo any permanent $CO_2$ induced changes. Measurements were performed at 30°C, 40°C

and 50°C and repeated three times on the same film and again on a second film to verify the values.

6FDA-DAM:DABA(4:1) hollow fibers were assembled into 20cm long shell-and-tube modules with 5-6 fibers each and the permeance of the fibers was tested using pure gas measurements in a constant pressure system – testing multiple modules of each state [15]. To simulate flue gas conditions, feed pressures of 20 psia were used. If found necessary, the fibers were post-treated with a 3wt% high molecular weight polydimethylsiloxane (PDMS) solution in heptane to seal any pinhole defects in the selective skin layer [17]. Mixed gas measurements using 20mol% $CO_2/N_2$ mixture feed on the shell side at 30°C, 40°C, and 50°C. A feed pressure of 100 psia was used to generate sufficient permeate for sampling (flow measured using a bubble flow meter and composition analyzed via gas chromatography). The retentate flow rate was set such that the stage cut across the fiber was less than 3% [18].

Wet gas permeation measurements on the hollow fibers membranes were made by saturating pure $CO_2$ or pure $N_2$ with a custom-built gas saturating system. The humidity of the feed gas was set to 80% RH (the maximum capabilities of the system) and supplied to the shell side of the fibers, using a needle valve to set the retentate flow rate to 740 mL/min and provide a feed pressure of 20 psia. The permeate humidity was monitored using a humidity meter and the permeate flow rate was measured using a bubble flow meter.

*Sorption*

The apparent heat of sorption, $H_{s,i}$, of $CO_2$ and $N_2$ can be determined using the van't Hoff temperature dependence of the gas sorption coefficients in polymeric materials,

$$S_i = S_{i,0} \exp\left(\frac{-H_{s,i}}{RT}\right) \tag{3.5}$$

where $S_{i,0}$ is the exponential pre-factor. The heat of sorption can be used to gauge the interaction between the gas penetrant and the polymer, where more negative values indicate stronger attractions between the pair. Using the piezometric method known as as "pressure decay" sorption, $CO_2$ and $N_2$ sorption isotherms in 6FDA-DAM:DABA(4:1) were obtained [19].

A VTI-SA vapor sorption analyzer from TA Instruments was used to obtain vapor adsorption equilibria on both pure and mixed matrix 6FDA-DAM:DABA(4:1) films at 30°C. The vapor activity was controlled by mixing wet vapor feeds with a dry $N_2$ line. The sample's "dry mass" was measured under $N_2$ and were at equilibrium before introduction of the vapors into the sample chamber.

### *3.3. Results and Discussion*

#### *Polymer synthesis*

As detailed in the *J.M.S.* paper [14], DSC and TGA revealed the synthesized 6FDA-DAM:DABA(4:1) has a glass transition and decomposition temperatures of 380°C and 450°C, respectively – results constant with other 6FDA-based polyimides [7,9]. Gel permeation chromatography (GPC) revealed the polymer has a molecular weight of 80,200 g/mol with a 2.35 polydispersity index.

#### *Sorption*

The $CO_2$ and $N_2$ sorption isotherms at relevant temperatures and pressures are shown in Figure 3.2. Based on the secant slope of these isotherms (between 0 and 10 psia), the solubility coefficients for $CO_2$ and $N_2$ sorption into 6FDA-DAM:DABA(4:1) were calculated with the solubility selectivity summarized in Table 3.II. For the temperatures investigated here, the

$CO_2/N_2$ solubility selectivity was found to be approximately 6, with a heat of sorptions for $CO_2$ of -28.3 ± 1.2 kJ/mol and -22.7 ± 1.4 kJ/mol (Table 3.II). As expected, these results indicate that the solubility selectivity will decrease with increasing temperature, indicating operation of the post combustion unit at lower temperatures will result in the most favorable sorption selectivites. When compared to other 6FDA-based polymer the more negative heat of sorption implies a stronger attraction between the $CO_2$ and the polymer matrix, either as a result of a more open structure or the free carboxylic acid in the polymer backbone.

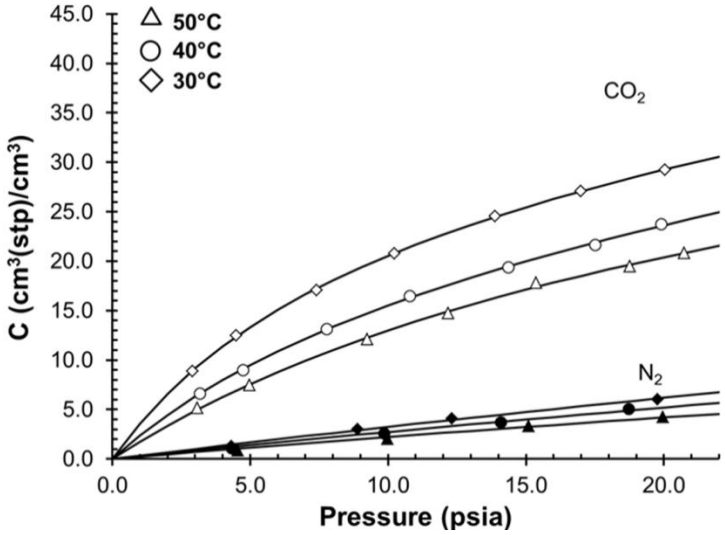


**Figure 3.2.** $CO_2$ and $N_2$ pure gas sorption isotherms on annealed 6FDA-DAM-DABA(4:1) at 30C, 40C, and 50C.

*Dense film permeation*

Table 3.II shows the $CO_2/N_2$ permeability and permselectivities at relevant temperatures and pressures. No significant pressure dependent-changes in permeability and permselectivity were observed between the tested pressures (5 to 20 psia). Using the sorption diffusion model (Equation 3.1), the diffusion coefficients were calculated using the gas permeability obtained from the dense film permeation experiments and the solubility coefficients from the sorption

isotherms. The activation energy of permeation, diffusion, and sorption for both $CO_2$ and $N_2$ were calculated using Equations 3.3, 3.4, and 3.5 respectively and are summarized in Table 3.II.

**Table 3.II**. Sorption and transport properties of 6FDA-DAM:DABA(4:1) at pressures < 20 psia.

| T(°C) | $D_{CO2}$ [$cm^2/s$] | $D_{CO2}/D_{N2}$ | $S_{CO2}/S_{N2}$ | $P_{CO2}$ (10 psia) [Barrers] | $P_{CO2}/P_{N2}$ |
|---|---|---|---|---|---|
| 30 | $5.4 \times 10^{-8}$ | 3.4 | 6.2 | 211.4 ± 0.3 | 21.3 |
| 40 | $7.5 \times 10^{-8}$ | 3.3 | 5.7 | 224.1 ± 0.5 | 20.4 |
| 50 | $9.7 \times 10^{-8}$ | 3.2 | 5.9 | 242.9 ± 2 | 19.4 |

As expected, the observed $CO_2$ permeability of 6FDA-DAM:DABA(4:1) sits below the 2008 polymer upper bound between 6FDA-DAM and 6FDA-DAM:DABA(2:1) [9, RWBaker2008]. The rubbery polymer tend to dominate the upper bound due to their large solubility selectivity and high permeabilities. The activation energy of permeability of $CO_2$ was found to be both positive and nearly 35% lower than that of $N_2$, indicating permeability will increase with increasing temperature. With the reverse trend being true for sorption, these results indicate sorption and diffusion have competing temperature dependencies, diffusion being the dominating factor. The negative difference between the activation energy of permeation between $CO_2$ and $N_2$ indicates an increase in temperature will result in a decrease in permselectivity (Table 3.II).

The diffusion selectivity was found to be approximately 3.3 for all tested temperatures with the diffusion coefficient for $CO_2$ almost doubling between 30°C and 50°C. While non-DABA-containing polyimides typically have a higher activation energy of diffusion for $N_2$ ($E_{D,N2}$), reflecting the large size of $N_2$, the activation energy of diffusion for both $CO_2$ and $N_2$ in 6FDA-DAM:DABA(4:1) were found to be very similar [16].

**Table 3.III**. Temperature dependent properties of 6FDA-DAM:DABA(4:1) films and fibers and $CO_2/N_2$ permselectivities at 30°C.

| | Flim | | | | Fiber | |
|---|---|---|---|---|---|---|
| | $E_P$ [kJ/mol] (200C annealed) | $H_s$ [kJ/mol] | $E_D$ [kJ/mol] | $\alpha_{CO2/N2}$ | $E_P$ [kJ/mol] (110C annealed) | $\alpha_{CO2/N2}$ |
| **$CO_2$** | 6.2 ± 0.5 | -28.3 ± 1.2 | 34.5 ± 1.7 | 20.8 | 8.2 ± 1.2 | 23.5 |
| **$N_2$** | 9.63 ± 0.8 | -22.7 ± 1.4 | 32.3 ± 2.2 | | 11.1 ± 0.7 | |

Looking at the results as a whole, it appears that the primary driver for the separation of $CO_2$ and $N_2$ in 6FDA-DAM:DABA(4:1) is the solubility selectivity, rather than diffusion selectivity, making up approximately 2/3rds of the total permselectivity. These results are the reverse of other polyimides where for gas pairs such as $CO_2/O_2$, where the diffusion is the dominating factor. The dominating solubility selectivity of $CO_2/N_2$ in 6FDA-DAM:DABA(4:1) is most likely due to the pendant carboxylic acid group on the DABA constituent of the polymer, which exerts both an induced dipole interaction and hydrogen bonding force with the quadrupoles and lone pairs of $CO_2$ [20]. Less interaction with $N_2$ and the carboxylic acid is likely due to the weak quadrupoles and lower critical temperature of $N_2$. At higher temperatures, the interaction between $CO_2$ and the carboxylic acid group will become weaker at higher temperatures, thus decreasing the solubility of $CO_2$ in the polymer matrix and the overall selectivity of the polymer. With the goal of maintaining a selectivity of at least 20 with a high $CO_2$ permeability, a 40°C operating temperature is appropriate.

*Hollow fiber spinning and permeation*

Utilizing an optimized spinning procedure developed for 6FDA-DAM:DABA(3:2), defect-free 6FDA-DAM:DABA(4:1) hollow fibers were spun by varying the air gap from 2 cm to 16 cm [6]. The resulting fibers had inner and outer diameters of approximately 257 μm and

130 μm, respectively. Defect-free fibers were achieved using an air gap of 2 cm (0.024 s gap residence time). As shown in Figure 3.3, a decrease in the ideal $CO_2/N_2$ selectivity was observed with an increase residence time in the air gap. It is hypothesized that interfacial phase separation occurred in the air gap due to greater moister absorption occurring as the residence time in the air gap increased. The effect was found to be "repairable" with a standard PDMS post-treatment used to repair pin-hole defects in the selective layer [17].

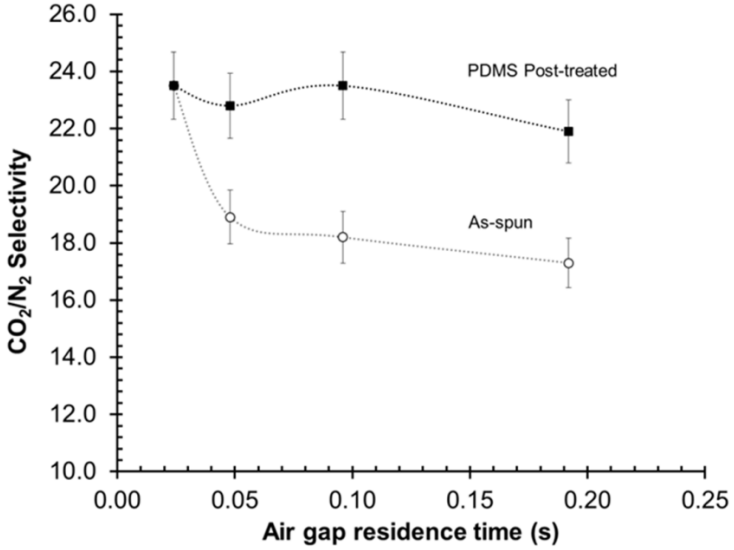


**Figure 3.3.** Ideal $CO_2/N_2$ permselectivites of 6FDA-DAM:DABA(4:1) hollow fiber membranes at 30C as a function of nascent fiber residence time in the air gap. Open circles represent as-spun fibers, where black circles fibers that have been post-treated with PDMS. Error bars represent one standard devation away from the average of multiple modules.

Using Equation 3.6 to approximate the skin layer thickness of the hollow fibers, the trends in Figure 3.4 were observed.

$$\ell = \frac{(Permeability)_i}{(Permeance)_i} \tag{3.6}$$

The skin layer appears to asymptote at approximately 800 nm at the residence time of the air gap is increased beyond 0.10 s. The evaporation of the volatile solvents and non-solvents from the

surface of the nascent fiber essentially dictates the skin thickness of the asymmetric membrane. Assuming Fickian diffusion and subsequent evaporation of solvents and non-solvents out of the nascent fiber skin layer, this asymptote is expected. The evaporation rate of the solvent and non-solvent will decrease with the square of the skin layer's increasing thinkness (assuming a constant solvent diffusion coefficient), thus essentially "self-limiting" the growth of the skin layer. Figure 3.5 shows a representative SEM image of a defect free skin layer of approximately 400 nm, as well as a transition region and the porous support beneath the skin.

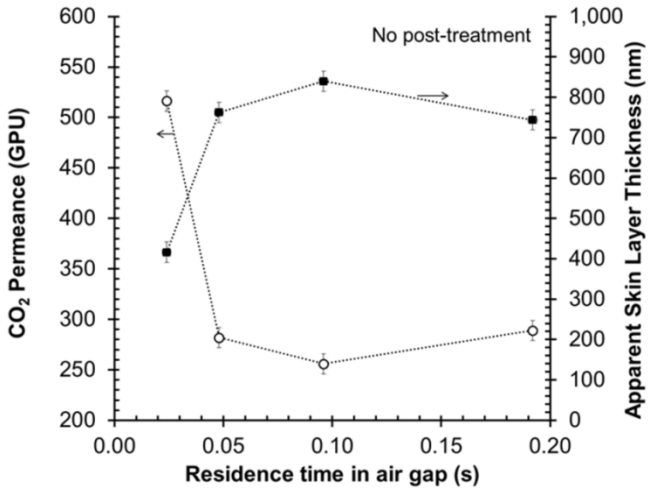


**Figure 3.4.** $CO_2$ permeance (open circles) and apparent skin layer thickness (black squares) of 6FDA-DAM:DABA(4:1) hollow fiber membranes. Error bars represent one standard deviation away from the average of multiple modules.

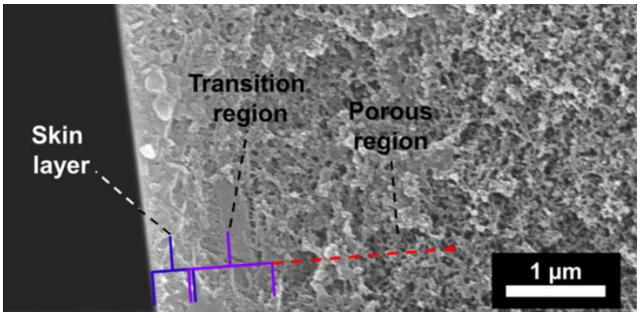


**Figure 3.5.** Representative SEM micrograph of defect-free 6FDA-DAM:DABA(4:1) hollow fiber membrane skin.

*Hollow fiber permeance and activation energy of permeation*

The defect-free hollow fibers were found to have a pure $CO_2$ permeance of approximately 520 ± 9 GPU [ 1 GPU = $10^{-6}$ $cm^3$(STP)/$cm^2$-s-cmHg], within a factor of two of the Polaris™ membrane (1000 GPU) [8]. As shown in Figure 3.4, the $CO_2$ permeance decreased with increasing air gap residence time, leveling off at approximately 290 ± 5 GPU. Using the permeation measurements at the various temperatures, the activation energy of permeation in the hollow fibers was calculated and included in Table 3.III. The activation energies of the hollow fibers were found to be higher than the dense films, implying that the "activated state" required more energy to permeate in the fibers than in the dense films.

The ideal $CO_2/N_2$ permselectivity of the 6FDA-DAM:DABA(4:1) hollow fiber membranes was found to be 23.5 at 30°C, higher than the dense film results (20.8). This phenomenon has been seen before in 6FDA-based polymer spinning and is most likely due to uniaxial orientation of the polyimide chains resulting from extremely high shear rates in the spinneret combined with rapid fiber take-up rates. This oriented arrangement presumably results in tighter packing of the polymer chains, which leads to an increase in gas perselectivity over the un-aligned state and lower gas permeation through the selective layer – contributing to the higher activation energy of permeation in the fiber [5]. Nonetheless, the defect free fibers had pure $CO_2$ permeances of approximately 560 ± 6 GPU with an ideal gas $CO_2/N_2$ permselectivity of 21.0 at 40°C. For these fibers, the skin thickness 415 ± 10 nm was calculated, so continued optimization of the spin dope and spinning conditions is required to reduce the skin thickness further.

*Mixed gas and wet gas permeation*

To simulate the $CO_2$-enriched flue gas found in the two-step counter-flow/sweep arrangement, a 20 mol% $CO_2$/80 mol% $N_2$ mixed gas feed was used to make non-ideal permeation measurements on the defect-free 6FDA-DAM:DABA(4:1) hollow fibers. The $CO_2$ permeance and $CO_2/N_2$ permselectivites measured under these conditions are summarized in Table 3.IV, along with the wet pure gas results.

**Table 3.IV.** Mixed gas and wet gas permeances and permselectivites for defect-free 6FDA-DAM:DABA(4:1) hollow fiber membranes.

| **Mixed gas (20 mol% $CO_2$)** | **$P_{CO2}$ (GPU)** | **$P_{CO2}/P_{N2}$** |
|---|---|---|
| 30 C | 320 ± 5 | 19.7 |
| 40 C | 381 ± 4 | 17.3 |
| 50 C | 400 ± 5 | 15.2 |
| **Wet gas (ideal, 80% RH)** | | |
| 30 C | 243 ± 2 | 20.9 |

With mixed gas feed, both the $CO_2$ permeance and permselectivity were found to be lower than pure gas experiments, likely indicating competitive sorption effects favoring nitrogen. An increase in temperature from 30°C to 50°C reduced the permselectivity by 22% with a 20% increase in permeance. While an increase in permeance in favorable, maintaining a selectivity of at least 20 is desirable to keep membranes costs from escalating dramatically.

Relative to dry $CO_2$ feeds, 6FDA-DAM:DABA(4:1) hollow fiber membranes were found to have significantly reduced $CO_2$ permeances when wet feeds (80% RH) were used. The likely cause of this permeace reduction is strong water sorption in the unrelaxed volume of the glassy polymer, resulting in a decrease in $CO_2$ sorption in the polymer [21]. Condensation of water in the nano-pores of the fibers sub-structure could have also contributed to the decrease in $CO_2$ permeance [22]. The permselectivity, however, was only slightly lower than that found in the dry pure gas experiments, presumably due to water out competing $CO_2$ for sorption sites. While the

loss of $CO_2$ performance due to water is significant, the permeance of the 6FDA-DAM:DABA(4:1) hollow fibers is still high relative to other polymers being considered. Additionally, further efforts to reduce the skin layer thickness to approximately 100 nm from 415 nm will result in permeances similar to MTR's Polaris™ membranes (1000 GPU), even in wet feeds [8].

*ZIF-8/6FDA-DAM:DABA(4:1) mixed matrix membranes*

When dispersing the ZIF-8 in the polymer solution using sonication, it was discovered that ecessive thermal energy input led to the formation of a non-flowing, insoluble gel. While ZIF-8 has demonstrated thermal stability and stability to basic solutions, it has been shown that the structure is susceptible to even weak acids [23, 24]. It is believe that the pendant carboxylic acid on the solvated 6FDA-DAM:DABA(4:1) chains destabilizes the exterior of the imidazole framework, subsequently inducing crosslinking between the polymer and ZIF particles. Casting of the mixed matrix films was achieved by minimizing the thermal energy input to the mixed matrix dopes, thus avoiding the undesired crosslinking effect.

XRD to compare the ZIF-8 power sample to the cast mixed matrix membrane and the crosslinked gel. As shown in Figure 3.6, the crystalline structure of ZIF-8 was maintained in the mixed matrix membrane when the crosslinking was avoided (b), whereas the intentionally gelled dope showed very poor crystallinity when compared to the ZIF-8 powder and the ZIF-8/6FDA-DAM:DABA(4:1) composite. Due to the fact that some crystallinity remains, it is believed that the ZIF-8 surface reacted with the carboxylic acid group on 6FDA-DAM:DABA(4:1), while the core of the partile likely remained crystalline.

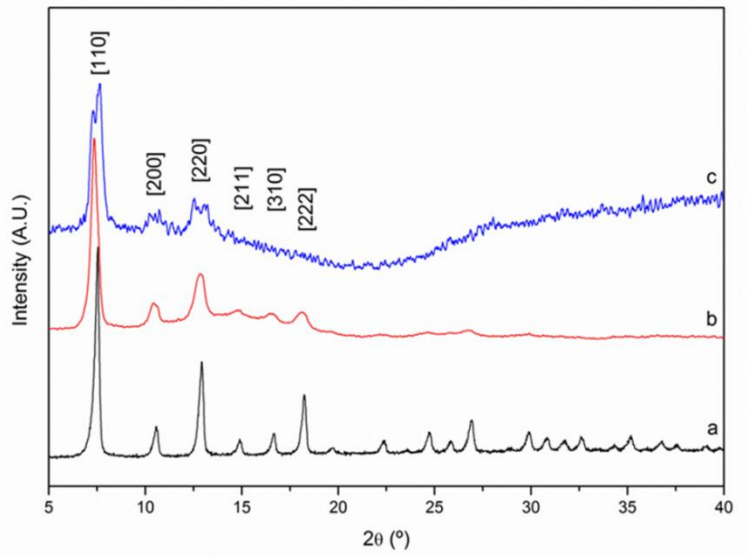


**Figure 3.6**. Powder X-ray diffraction patters for (a) ZIF-8 power, (b) 20 wt% ZIF-8/6FDA-DAM:DABA(4:1) film made with out sonication, and (c) flakes made of the gelled 20 wt% ZIF-8/6FDA-DAM:DABA(4:1) dope made with sonication.

SEM images of the 20 wt% ZIF-8/6FDA-DAM:DABA(4:1) composite membranes revealed a fairly homogenous dispersion of the ZIF-8 within the polymer matrix (Figure 3.7a). The ZIF-8 particles appeared to range from 40-150 nm, with the majority being 50 nm. SEM and TEM (Figure 3.7 b-d) both revealed relatively decent adhesion between the polymer and ZIF-8 particles. However, a minor portion of the dispersed ZIF-8 particles were agglomerated. These non-ideal regions will lead to higher, yet non-selective, fluxes and may also have small enough interparticle pores that could results in capillary condensation of water between particles.

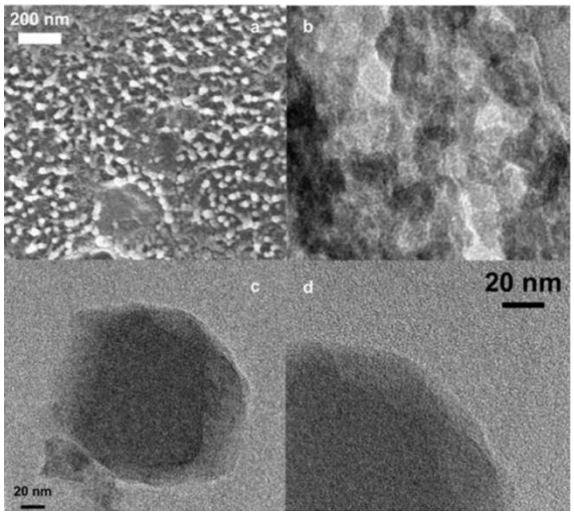


**Figure 3.7**. Representative SEM (a) and HRTEM (b-d) micrographs of 20 wt% ZIF-8/6FDA-DAM:DABA(4:1) mixed matrix membranes. (b) Small domains of aggregates were found, while (c) and (d) show good dispersion and adhesion of the ZIF particles (dark grey) in the 6FDA-DAM:DABA polymer matrix (light grey).

Pure gas permeation on the 20 wt% ZIF-8/6FDA-DAM:DABA(4:1) mixed matrix membrane showed a significant enhancement $CO_2$ permeability with only a minimal loss in $CO_2/N_2$ selectivity. As shown in Figure 3.8, the $CO_2$ permeability of the composite film was 553 ± 3 Barrers, 2.5x that of the neat polymer film with only a 9.3% decrease in $CO_2/N_2$ selectivity. With the adhesion and dispersion of the ZIF-8 particles within the polymer matrix, it appears that the loss in selectivity is a results of the intrinsic properties of the ZIF-8 (which only has a selectivity of approximately 10) [13]. While the loss in selectivity is not favorable, the 2.5x increase in permeability over the neat polymer more than offsets the 9.3% decrease. If ZIF-8/polymer membrane are made using 6FDA-based polymers (which has already been done with Ultem® as the polymer matrix), the resulting ultra-high flux fibers could be used to drastically reduce $CO_2$ capture costs [12].

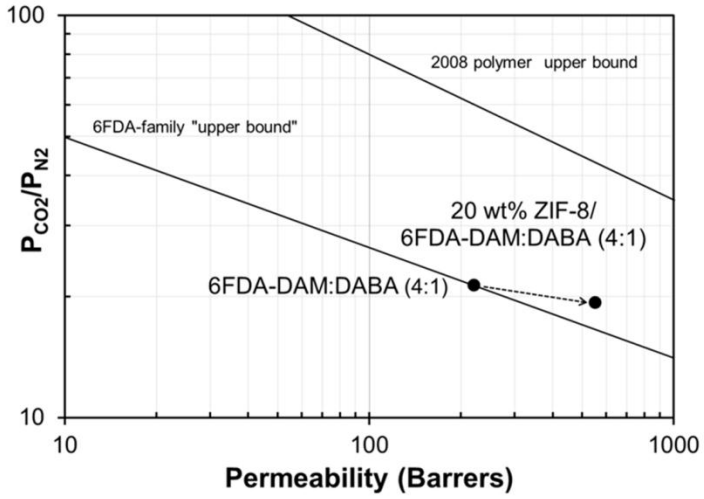


**Figure 3.8.** Robeson plot illustrating the effect of 20 wt% ZIF-8 addition to 6FDA-DAM:DABA(4:1) and a hypothetical 6FDA-family upper bound [25].

*3.4. Conclusions*

Using a process guided approach, 6FDA-DAM:DABA(4:1) hollow fibers membranes have been developed for $CO_2$ recovery from post-combustion flue gas. $CO_2$ permeances of 520 ± 9 GPU with ideal $CO_2/N_2$ permselectivites of 23.5 were obtained at 30°C for defect free fibers with 415 ± 10 nm apparent skin thickness. Mixed gas and wet gas experiments showed a significant reduction in $CO_2$ permeance at 30°C and a loss in selectivity at 40°C, indicating the optimum operation temperature exists between 30°C and 40°C. Even though the mixed gas and wet gas feeds reduced the $CO_2$ permeance, incorporating ZIF-8 into the 6FDA-DAM:DABA(4:1) polymer matrix at 20 wt% resulted in a 2.5x increase in permeance with only a 9.3% loss in selectivity. With further optimization of the spinning process to produce fibers with a 100 nm skin thickness, mixed matrix membranes of 20 wt% ZIF-8 in 6FDA-DAM:DABA(4:1) could potentially have wet $CO_2$ permeances of approximately 2000 GPU and a $CO_2/N_2$ permselectivities of approximately 19.5.

**REFERENCES**


1. Annual Energy Outlook 2012, Energy Information Administration, Report no. DOE/EIA-0383ER, 2012
2. H Lin, BD Freeman. Gas solubility, diffusivity and permeability in poly(ethylene oxide). *Journal of Membrane Science,* 2004. 239 p. 105–117.
3. KI Okamoto, N Umeo, S Okamyo, . Tanaka, H Kita. Selective permeation of carbon dioxide over nitrogen through polyethyleneoxide-containing polyimide membranes. *Chemistry Letters*, 1993. 22 p. 225–228.
4. CJ Orme, MK Harrup, TA Luther, RP Lash, KS Houston, DH Weinkauf, FF Stewart. Characterization of gas transport in selected rubbery amorphous polyphosphazene membranes. *Journal of Membrane* Science, 2001. 186 p. 249–256.
5. TS Chung, WH Lin, RH Vora. The effect of shear rates on gas separation performance of 6FDA-durene polyimide hollow fibers. *Journal of Membrane Science*, 2000. 167 p. 55–66.
6. IC Omole, RT Adams, SJ Miller, WJ Koros. Effects of CO2 on a high performance hollow-fiber membrane for natural gas purification. *Ind. Eng. Chem. Res*, 2010 49 p. 4887–4896.
7. C-C. Chen, W. Qiu, S.J. Miller, W.J. Koros. Plasticization-resistant hollow fiber membranes for CO2/CH4 separation based on a thermally crosslinkable polyimide. *J. Membr. Sci.*, 382 (2011), pp. 212–221.
8. T.C. Merkel, H. Lin, X. Wei, R. Baker. Power plant post-combustion carbon dioxide capture: an opportunity for membranes. *J. Membr. Sci.*, 359 (2010), pp. 126–139
9. JH Kim, WJ Koros, and DR Paul. Effects of $CO_2$ exposure and physical ageing on crosslinking. *Journal of Membrane Science*, 2006. (282) p 32 – 43.
10. W Qiu, CC Chen. L Xu. WJ Koros. Effects of polyimide chemical structure on membrane gas separation performance. *Proceedings of the North American Membrane Society*. Annual Meeting, New Orleans, LA. June 13 2012.
11. J.C.S. Remi, T. Rémy, V. Van Hunskerken, S. van de Perre, T. Duerinck, M. Maes, D. De Vos, E. Gobechiya, C.E.A Kirschhock, G.V. Baron, J.F.M. Denayer. Biobutanol separation with the metal-organic framework ZIF-8. *ChemSusChem*, 4 (2011), pp. 1074–1077.

12. Y Dai, et al. Ultem/ZIF-8 mixed matrix hollow fiber membranes for $CO_2/N_2$ separations. *Journal of Membrane Science*, 2012.
13. C. Zhang, Y. Dai, J.R. Johnson, O. Karvan, W.J. Koros. High performance ZIF-8/6FDA–DAM mixed matrix membrane for propylene/propane separations. *J. Membr. Sci*, 389 (2012), pp. 34–42.
14. RP Lively, et al. A high-flux polyimide hollow fiber membrane to minimize footprint and energy penalty for CO2 recovery from flue gas. *J. Membr. Sci.* 423 – 424 (2012), pp. 302 – 313.
15. T. Moore, S. Damle, P. Williams, W.J. Koros. Characterization of low permeability gas separation membranes and barrier materials; design and operation considerations. *J. Membr. Sci*, 245 (2004), pp. 227–231.
16. L.M. Costello, W.J. Koros. Thermally stable polyimide isomers for membrane-based gas separations at elevated temperatures. *J. Polym. Sci.* B, 33 (1995), pp. 135–146.
17. S. Husain, Mixed Matrix Dual Layer Hollow Fiber Membranes for Natural Gas Separation, Ph.D. Dissertation, Georgia Institute of Technology, Atlanta, GA, 2006.
18. D.W. Wallace, Crosslinked Hollow Fiber Membranes for Natural Gas Purification and their manufacture from novel polymers, Ph.D. Dissertation, in: Chemical Engineering, The University of Texas at Austin, Austin, TX, 2004.
19. W.J. Koros, D.R. Paul. Design considerations for measurement of gas sorption in polymers by pressure decay. *J. Polym. Sci., Polym. Phys. Ed*., 14 (1976), pp. 1903–1907.
20. A. Torrisi, C. Mellot-Draznieks, R.G. Bell. Impact of ligands on CO2 adsorption in metal-organic frameworks: First principles study of the interaction of CO2 with functionalized benzenes. II. Effect of polar and acidic substituents. *J. Chem. Phys.*, 132 (2010), p. 044705.
21. D.K. Yang, W.J. Koros, H.B. Hopfenberg, V.T. Stannett. Sorption and transport studies of water in kapton polyimide. I. *J. Appl. Polym. Sci*., 30 (1985), pp. 1035–1047.
22. G.Q. Chen, C.A. Scholes, G.G. Qiao, S.E. Kentish. Water vapor permeation in polyimide membranes. *J. Membr. Sci*., 379 (2011), pp. 479–487.
23. K.S. Park, Z. Ni, A.P. Coˇte, J.Y. Choi, R. Huang, F.J. Uribe-Romo, H.K. Chae, M. O'Keeffe, O.M. Yaghi. Exceptional chemical and thermal stability of zeolitic imidazolate frameworks. *Proc. Nat. Acad. Sci. USA*, 103 (2006), pp. 10186–10191.

24. J.A. Thompson, C.R. Blad, N.A. Brunelli, M.E. Lydon, R.P. Lively, C.W. Jones, S. Nair. Hybrid zeolitic imidazolate frameworks: controlling framework porosity and functionality by mixed-linker synthesis. *Chem. Mater.*, 24 (2012), pp. 1930–1936.
25. L.M. Robeson. The upper bound revisited. *J. Membr. Sci.*, 320 (2008), pp. 390–400.

# CHAPTER 4

# WATER AND ETHANOL ADSORPTION IN METHANOL-DERIVED ZIF-71

## *4.1. Introduction*

Due to the favorable size difference between $CO_2$ and $N_2$ – 0.33 nm for $CO_2$ and 0.36 nm for $N_2$ – $CO_2$ selective materials can be chosen based on pore size and therefore their diffusive selectivity. Unfortunately, this approach cannot be used when selecting ethanol selective materials for ethanol/water separations – 0.45 nm for ethanol and 0.27 nm for water. For this separation, hydrophobic materials with high ethanol/water sorption selectivities are desired.

Recently, hydrophobic zeolitic imidazolate frameworks (ZIFs) have been used for a variety of applications, including $CO_2$ capture and hydrogen storage [1, 2]. ZIFs are a class of metal organic framework (MOF) that are formed by the coordination between metal centers and organic imidazole links [2]. When compared to most MOFs, ZIFs have been shown to have high chemical and thermal stability, as well as possess permanent porosity [3]. Using grand canonical Monte Carlo methods, Nalaparaju et al. identified ZIF-71 (a ZIF comprised of zinc metal centers and 4,5-dichloroimidazole ligands), as having high ethanol water selectivities (between 300 and 400) for low ethanol concentrations [4]. These predicted selectivities are significantly higher than standard hydrophobic sorbents currently in use [5].

The remainder of this chapter has been adapted from the work published in *Chemical Communications* and demonstrates a straightforward and effective synthesis route for ZIF-71 as well as an experimental comparison to Nalaparaju et al.'s modeling work.

*4.2 Materials and Methods*

*Synthesis*

ZIF-71 was prepared by mixing a solution of metal center and a solution of the imidazole linker in a scintillation vial. A solution of zinc acetate (0.0743 g, 0.40 mmol) in 15 mL of methanol and a solution of 4,5-dichloroimidazole (dcIm, 0.2192 g, 1.60 mmol) in 15 mL of methanol, were combined in a sealed vial and allowed to stand at room temperature for 24 h. The methanol was then decanted off, and the remaining crystals were washed with 20 mL of chloroform for 3 days, refreshing the chloroform each day. After 3 days, the solution was centrifuged to recover the crystals and then dried under vacuum at 50°C for 24 h to remove any remaining solvent. Near quantitative yields (0.137 g) of ZIF-71 were recovered after solvent exchange and drying. This reaction was repeated 5 times with similar results.

*Characterization*

The resulting crystals were examined using PXRD, SEM, $N_2$ physisorption, TGA, ethanol and water vapor adsorption, and FT-IR. Powder X-ray diffraction patterns were obtained on a PAnalytical X'pert diffractometer operating with Cu Kα radiation and equipped with an X'celerator detector. Prior to examining the crystals with a scanning electron microscope (SEM), the ZIF-71 crystals were sputter coated with an 10-20 nm thick gold coating (Model P-S1, ISI, Mountain View, CA). A high resolution Field Emission Scanning Electron Microscope, Leo 1530 (Leo Electron Microscopy, Cambridge, UK) was used to obtain the SEM images. Brunauer-Emmett-Teller (BET) surface areas and micropore volumes (t-plot method) were calculated from $N_2$ physisorption measurments performed on an ASAP 2020 (Micrometrics), degassing the sample at 200°C for 18 h within the apparatus prior to testing. A Netzsch STA 409

TGA with temperature programming capabilities (ramp of 10°C/min to 700°C from room temperature) was used to obtain mass loss and derivative mass loss as a function of temperature.

Ethanol and water vapor sorption measurements were obtained using a custom-made McBain quartz-spring sorption system with an optical level reader (cathetometer). This gravimetric technique involves supporting a sample of known weight on a calibrated quartz spring (GE Sensing, Houston, TX) within a temperature controlled chamber. The sample was held at 35°C while the manifold leading to the sample was held at 45°C to prevent condensation. After evacuating the sample for 2 days and taking a reverence point on the scale, the sample was isolated and vapor source (ethanol or water) was degassed. Ethanol vapor was introduced to the sample first, allowing the pressure to increase a few torr for each measurement and recording time temperature, pressure, and reading on the cathetomer for each increase. With knowledge of the spring constant and the elongation of the spring, the total mass of sorbed vapor can be estimated. After ethanol sorption was completed, the sample and sample chamber were evacuated for 3 days, and the same procedure was repeated with water and then again with ethanol to ensure water sorption was reversible.

*4.3. Results and Discussion*

The powder diffraction patter of the methanol-derived ZIF-71 (Figure 4.1, a) matches well with previous dimethylformamide derived ZIF-71 synthesis and exhibits the expected RHO-type topology [1]. SEM images (Figure 4.1, b) reveal that the ZIF-71 crystals do not display a distinct morphology and can best be described as cubic. A particle size of approximately 1 μm was observed and appeared to be consistent throughout the sample.

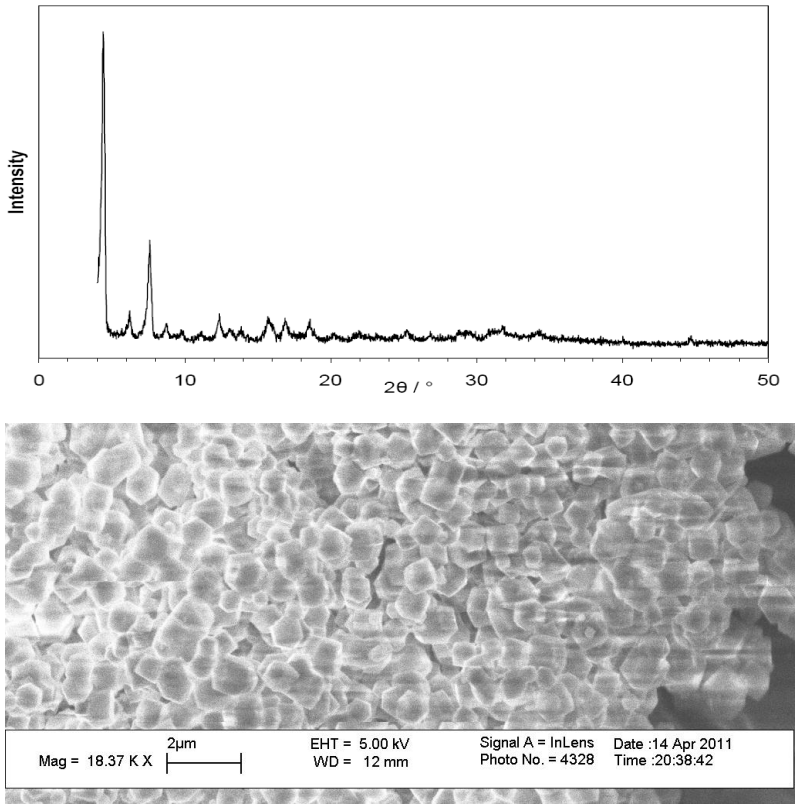


**Figure 4.1.** ZIF-71 synthesized in methanol at room temperature. (top) PXRD pattern and (bottom) SEM image.

$N_2$ physisorption experiments show a typical Type II isotherm with no noticeable hysteresis (Figure 4.2). Interestingly, higher than expected BET surface areas (1186.5 ± 27.8 $m^2g^{-1}$) and t-plot pore volumes (0.385 ± 0.010 $cm^3(STP)g^{-1}$) were observed. Previous synthesis routes, which use dimethylformamide (DMF) as the solvent, produced ZIF-71 crystals with a BET surface area of 652 $m^2g^{-1}$ [1]. The most likely explanation of the striking difference in surface area is the difference in solvent size (0.38 – 0.41 nm for methanol, and 0.52 – 0.55 nm for DMF) [6, 7]. When comparing the nominal pore window diameter of ZIF-71 (0.48 nm) and the kinetic diameter of DMF and methanol, it is apparent that DMF cannot easily evacuate from the cages via the pore windows [4]. While a careful solvent exchange procedure was used, it is likely that a significant amount of DMF remained within the pore structure whereas the methanol

could easily be removed. The remaining DMF in the pore structure likely contributed to the lower BET surface area observed for that synthesis route. A second hypothesis also focuses on the difficult removal of DMF from the ZIF pore structure. If the DMF is removed from the pores, it would require significant deformation of the crystal structure. It is conceivable that the deformation caused by the DMF removal caused a partial collapse of the ZIF structure, resulting in lower surface areas and limited access of the adsorbates to the collapsed cages. Presumably, any ZIF with a pore diameter less than the kinetic diameter of the solvent faces similar issues. Ongoing studies are aimed at distinguishing between these two hypotheses.

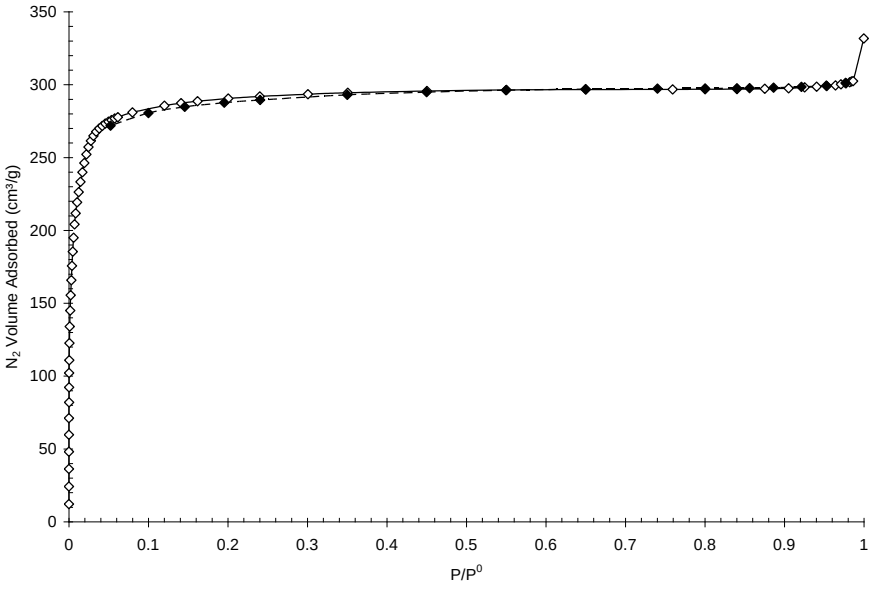


**Figure 4.2.** $N_2$ physisorption isotherm on ZIF-71. Open symbols denote adsorption, closed symbols denote desorption.

TGA results of the methanol-derived ZIF-71 (Figure 4.3) showed no noticeable mass loss between 100 – 200 C, indicating that water and other atmospheric gasses are minimally taken up by the ZIF. At 415°C, a large mass loss was observed and is most-likely associated with the decomposition of the ZIF.

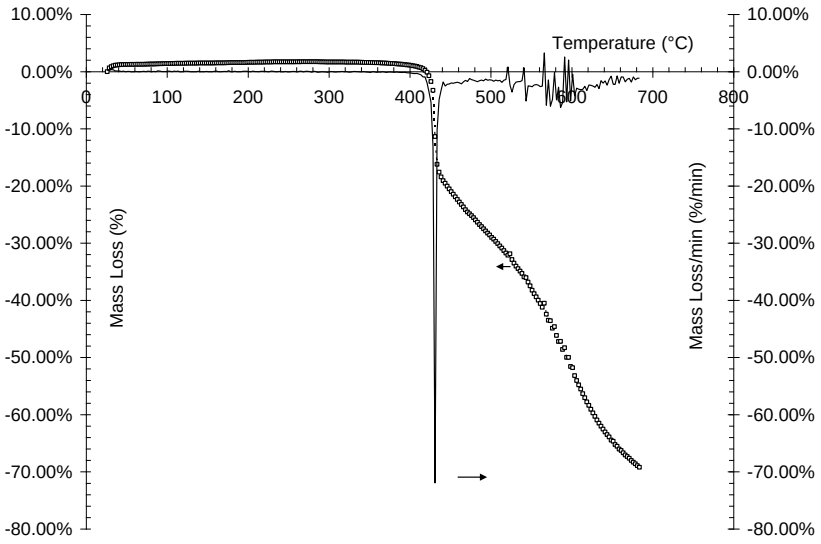


**Figure 4.3.** TGA results for methanol derived ZIF-71, showing mass loss and the derivative mass loss as a function of temperature.

Ethanol vapor uptake into ZIF-71 exhibits a typical Type IV isotherm (Figure 4.4), which is indicative of monolayer adsorption at low pressures followed by capillary condensation at a higher activity ($P_{EtOH}/P^*_{EtOH}$ = 0.135, $P_{EtOH}$ = 13.9 mmHg of ethanol). A slight adsorption hysteresis is observed, which is typical of pore-filling/evacuation cycles [8]. Water uptake into ZIF-71 exhibits a Type I isotherm low pressures and is significantly less than silicalite-1 [9, 10]. As shown in Figure 4.4, the water uptake in ZIF-71 is significantly less than the ethanol uptake with no observed capillary condensation point. For vapor phase separations, the ideal ethanol/water selectivity of a sorbent can be estimated vai:

$$\alpha_{E/W} = \frac{C_{sorbed,ethanol}}{C_{vapor,ethanol}} \div \frac{C_{sorbed,water}}{C_{vapor,water}} \quad (1)$$

For a vapor feed of 9.4% ethanol activity and 90.6% water activity, the ethanol/water selectivity of ZIF-71 is estimated to be 11.1, using the pure vapor data from Figure 4.4.

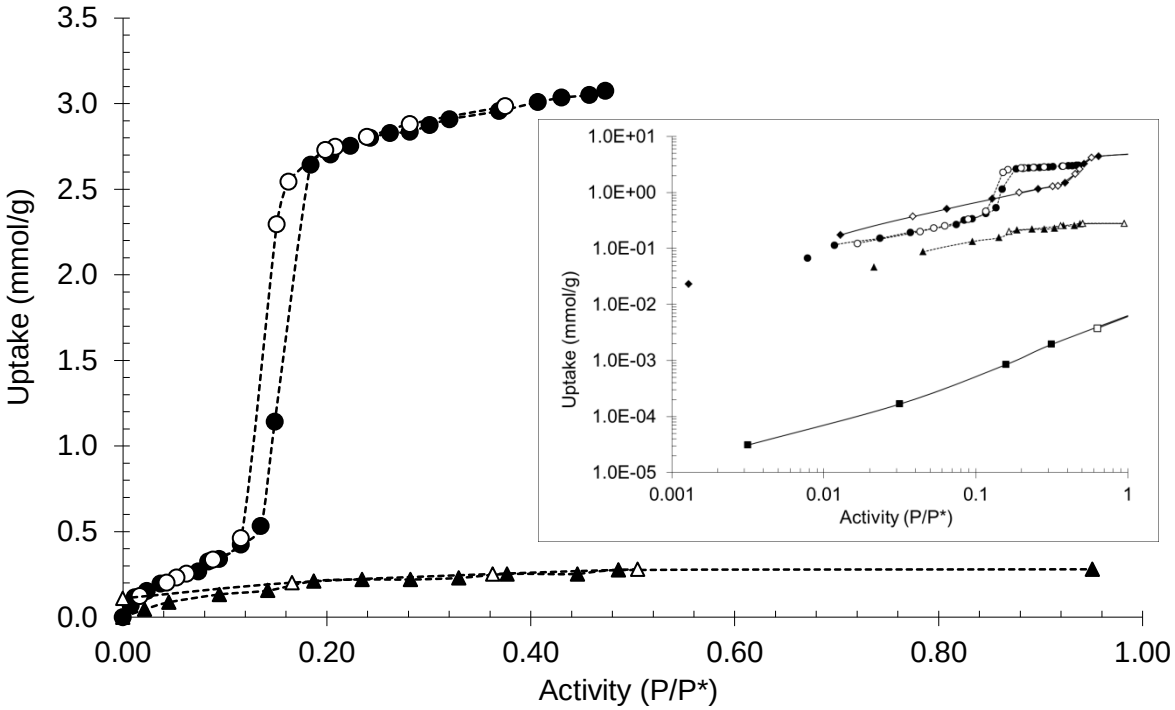


**Figure 4.4.** Pure vapor ethanol (circles) and water (triangles) isotherms for ZIF-71 at 35°C. Adsorption is denoted by filled symbols while desorption is denoted by open symbols. (inset) Comparison with the models predicted at 25°C [4]. Ethanol prediction (diamonds), water predictions (squares).

The pure vapor sorption isotherms were compared to the recent grand canonical Monte Carlo simulation study that was carried out at 25°C (Figure 4.4, inset) [4]. The predicted ethanol isotherm compares well with the experimental measurements studied here, with only a few discrepancies. The difference in the total uptake between the simulations and the experiment can likely be attributed to the difference in temperature used in the two studies. Additionally, the capillary condensation point is predicted to be a 7 mmHg higher than was actually observed, which corresponds to a difference of greater than 200% in activity. The difference in this point likely arises in the model due to the use of a stationary ZIF framework as well as the known over-prediction of saturated vapor pressure when transferable potentials for phase equilibria (TraPPE) force fields are used [11]. The most notable difference lies in the almost two order of

magnitude difference between the predicted water uptake and the measured water uptake. It is likely that this higher than predicted water uptake is the result of an additional adsorption mechanism not considered by the authors of the modeling study.

While it is reasonable to conclude that the inner network of ZIF-71 is hydrophobic, the same cannot necessarily be said for the outer surface of the crystal. Without going into any specific adsorbate-sorbent interactions, a simple calculation assuming monolayer coverage of water on the outside of the crystal (assuming 1 μm crystals and 0.29 nm water molecules packing as spheres) yields the weight-normalized loading of water that might be observed in the water uptake experiments. As a simple proof-of-concept, this estimated water uptake was added to the grand canonical Monte Carlo water uptake prediction (Figure 4.5). The close agreement between the "adjusted" model and the experimental data lends support to the hypothesis of additional water adsorption on the crystal surface.

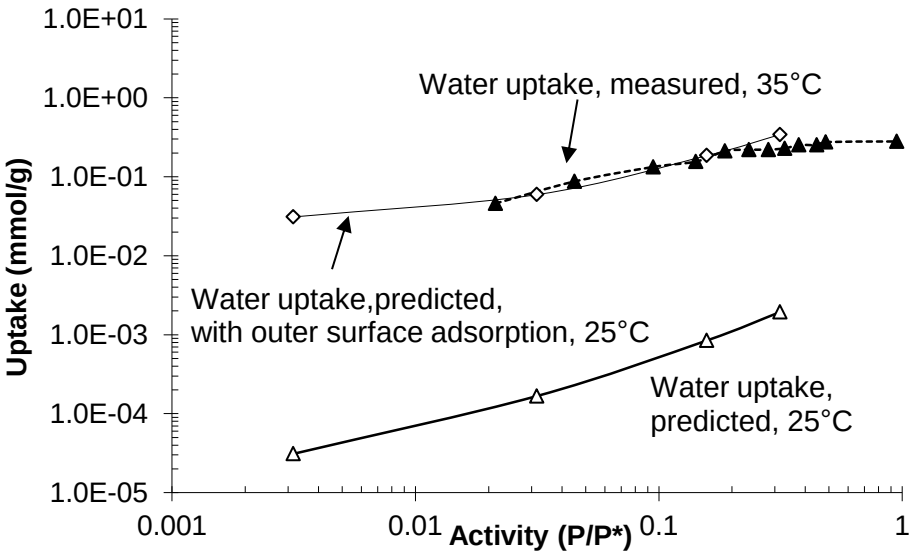


**Figure 4.5.** Comparison of water uptake in ZIF-71. Experimental water uptake (closed triangles), Monte Carlo predictions [4] (open triangles), predictions with outer surface adsorption included (open diamonds).

While it is difficult to elucidate an adsorption mechanism at this time, an initial hypothesis is provided. It is presumed that during the synthesis of ZIF-71, excess dcIm used in the reaction results in dcIm terminated crystals. In order for a terminal zinc atom to be charge balanced, an unconjugated lone pair of neutral dcIm in solution will attack the partially positive zinc (Figure 4.6). This terminal linker introduces a –N–H functionality to the surface of the crystal, thus allowing hydrogen bonding with the vapor phase water and the formation of low pressure monolayers. FTIR spectra of the dried ZIF-71 crystals (Figure 4.7), revealed a distinct peak at 3419 $cm^{-1}$ that is assigned to a hydrogen bonded N–H stretch [12]. Additional studies varying the crystal size and/or chemical modification of the outer surface are necessary to confirm this hypothesis.

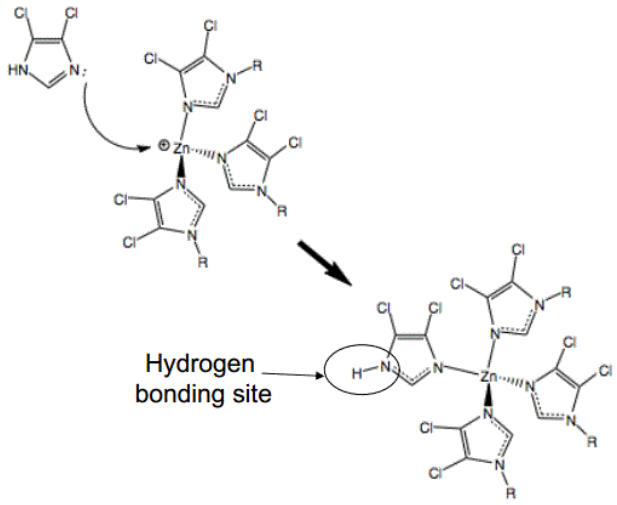


**Figure 4.6.** ZIF-71 crystal termination via neutral dcIm. The resulting hydrogen bonding site is proposed to be responsible for the higher-than-expected water uptake in ZIF-71.

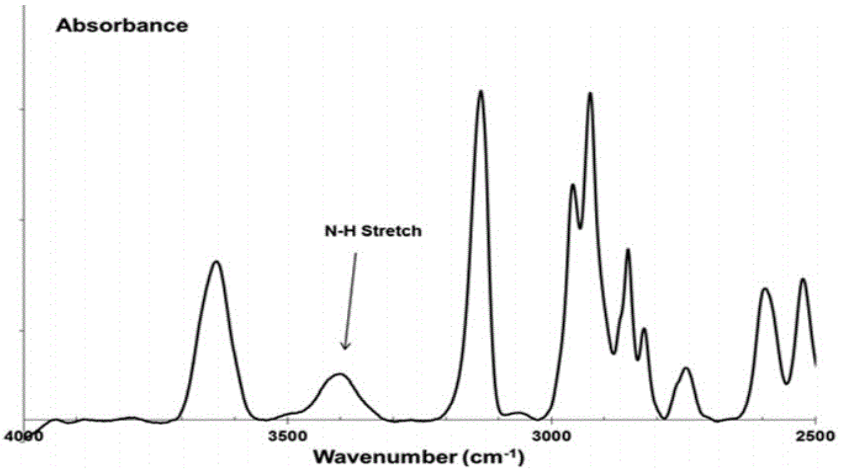


**Figure 4.7.** FT-IR spectra for ZIF-71 after solvent exchange and drying.

*4.4. Conclusion*

In conclusion, a new route has been developed to synthesize ZIF-71 with higher yields and significantly higher surface areas than previous methods. The higher observed surface areas are most likely due methanol being more easily removed (compared to DFM) from the ZIF pore structure. Pure vapor isotherms of ethanol and water were measured and compared to existing sorption predictions. An ethanol/water selectivity of 11.1 is estimated for a vapor feed of 9.4% ethanol activity and a 90.6% water activity. Higher than predicted water uptakes are observed and is most likely attributed an unaccounted for mechanism for outer surface water adsorption in the prediction model.

While the measured water uptake in ZIF-71 is less than that in silicalite-1, the minimal ethanol uptake at low activities significantly reduces its viability as a sorbent for the desired dilute ethanol feeds. This said, ZIF-71 has been incorporated into a PDMS matrix, the results of which have been reported in Chapter 6 of this work.

**REFERENCES**


1. W Morris, et al. A combined experimental-computational investication of carbon dioxide capture in a series of isoreticular zeolitic imidazolate frameworks. *J. Am. Chem. Soc.* 132 (2010) pp. 11006 – 11008.
2. H Wu, W Zhou, T Yildirim. Hydrogen storage in a prototypical zeolitic imidazolate framework-8. *J. Am. Chem. Soc.* 129 (2007) 5314-5315.
3. KS Park. Exceptional chemical and thermal stability of zeolitic imidazolate frameworks. *Proc. Natl. Acad. Sci. USA.*103 (2006) pp 10186 – 10191.
4. A Nalaparaju, X Zhao, and J Jiang. Molecular Understanding of the Adsorption of Water and Alcohols in Hydrophili and Hydrophobic Zeolitic Metal-Organic Frameworks. *The Journal of Physical Chemistry C*, 2010. 114(26) p 11542 – 11550.
5. T. Sano, H. Yanagishita, Y. Kiyozumi, F. Mizukami, K. Haraya. Separation of ethanol/water mixture by silicalite membrane on pervaporation. *J. Membr. Sci*., 95 (1994), p. 221.
6. ME vanLeewen, et al. Methanol kinetic diameter. *Fluid Phase Equlibrium. 99 (1994).*
7. J Sekulic, JE ten Elshof, and DHA Blank. Separation mechanism in dehydration of water/organic binary liquids by pervaporation through microporous silica. *Journal of membrane science*. 254, no. 1 (2005): 267-274.
8. J. Kloubeck. Hysteresis in porosimetry. *Powder Technology.* 29 (1981): 63-73.
9. M. Soulard, J. Patarin, V. Eroshenko, R.-C. Regis, Proc. Int. Zeolite Conf. 14th 2003, 2004, 1830.
10. A Giaya. Water confined in cylindrical micropores. *The Journal of chemical physics.* 117 (2002): 3464.
11. B. Chen, J Potoff, and JI Siepmann. Monte Carlo calculations for alcohols and their mixtures with alkanes. Transferable potentials for phase equilibria. 5. United-atom description of primary, secondary, and tertiary alcohols. *The Journal of Physical Chemistry B*. 105 (2001): 3093-3104.
12. M. K. Van Bael, J. Smets, K. Schoone, L. Houben, W. McCarthy, L. Adamowicz, M. J. Mowak and G. Maes, *J. Phys. Chem. A.* 101 (1997) p 2397–2413.


.

# CHAPTER 5

# TRANSPORT PROPERTIES OF ETHANOL AND WATER IN FLUORIDE MEDIATED SILICALITE-1

## *5.1. Introduction*

Silicalite-1, a pure silica MFI-type zeolite, is one of the most largely studied materials for extraction of ethanol from dilute aqueous mixtures. The MFI-type structure is comprised of a three-dimensional interconnected framework with a pore structure consisting of two channels: a straight channel with circular openings (0.54 x 0.56 nm) and a sinusoidal channel with elliptical openings (0.51 x 0.55 nm) [1-3]. MFI structures included both Al-containing commonly used ZSM-5 and pure silica (Al-free) silicalite. Silicalite-1, in particular, is ideally suited for this separation due to both the overall hydrophobic/organofillic nature of the framework.

Silicalite-1 is typically synthesized in alkaline conditions, using $OH^-$ as a mineralizing agent (referred to as silicalite-1($OH^-$) for the remainder of this work). This synthesis method tends to allow for the formation of considerable number of internal silanol defects. These defects can be formed on removal of the charge balancing centers for the template tetrapropalammonium and, in general, about 5% of the Si atoms in the framework are hydroxylated [4, 5]. Due to their slightly polar nature, these silanol defects are hydrophilic and therefore decrease the overall hydrophobicity. A nearly defect-free silicalite-1 framework can be obtained with an extremely low density of silanol defects by replacing the $OH^-$ with $F^-$ for the mineralizing agent and reacting at near neutral conditions (referred to as silicalite-1($F^-$) for the remainder of this work) [6, 7]. In this so-called fluoride route, the fluoride ions $F^-$ can offset the template ions such that fewer internal defects are formed [8-11]. As is shown in the remainder of this chapter, the

effective elimination of these internal silanol defects dramatically reduces the water uptake, especially at high water activity.

Due to the enhanced hydrophobicity of silicalite-1($F^-$) over silicalite-1($OH^-$), silicalite-1($F^-$) is an even better alternative for use in the extraction of ethanol from dilute aqueous mixtures (as are found in biofuel applications). This chapter reports the transport properties of ethanol and water in silicalite-1($F^-$) through the study of pure vapor adsorption and diffusion measurements. The remainder of this chapter has been adapted from the work published in *Langmuir* and *Microporous and Mesoporous Materials* [12, 13].

## *5.2. Materials and Methods*

### *Zeolite Synthesis*

Silicalite-1($OH^-$) was acquired from Sigma-Aldrich (particle size between 3-5 μm) and silicalite-1($F^-$) was prepared in a fluoride mediated route by hydrothermal synthesis adapted from literature procedures [6, 7, 14]. The ($OH^-$) and ($F^-$) naming system is based in reference to the mineralizing ion in the synthesis procedure (note that the $F^-$ ions are not incorporated into the silicalite-1 framework). Tetrapropylammonium bromide (TPABr, 1.62 g, 99% Sigma Aldrich) and ammonium fluoride ($NH_4F$, 0.116 g, >99.99% Sigma Aldrich, stored in a desicator) were dissolved in 26.88 g of DI water. In a 40 mL Teflon sleeve, 4.48 g of Cab-O-Sil M-5 (Cabot Corporation) was slowly added to the mixture, stirring manually for 10 min to ensure a homogenous gel was formed. The Teflon sleeve was then sealed in a tightly sealed stainless steel reactor (Parr Instruments) and transferred to a 180°C oven for 14 days. After cooling, the resulting solids were vacuum filtered and washed with 200 mL of DI water. To remove any unreacted, amorphous silica, 30 mL of DI water was added to the solids and then sonicated for

90 s. The slurry was then centrifuged and the water was decanted off. This sonication-centrifuged cycle was repeated a minimum of two more times. The crystals were then dried and calcined using the following profile: ramp 5°C/min, 120°C for 2h, ramp 5°C/min, 550°C for 12 h. The reaction yielded 3.4 g, a 76% yield based on silica, was achieved with an average crystal size of 70 µm x 30 µm x 15 µm (Figure 5.1).

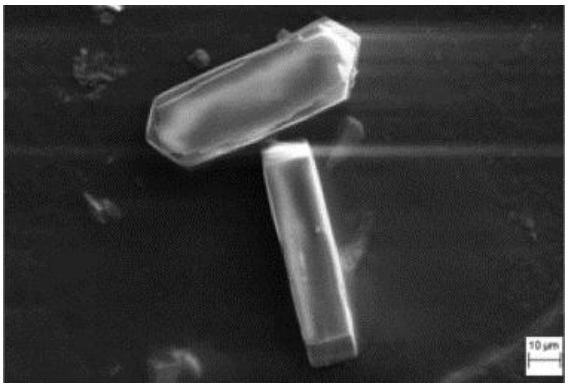


**Figure 5.1.** Silicalite-1($F^-$) crystals synthesized and used in this study.

*Characterization*

Brunauer-Emmett-Teller (BET) surface areas and micropore volumes (t-plot method) of silicalite-1($OH^-$) and silicalite-1($F^-$) were calculated from $N_2$ physisorption measurments performed on an ASAP 2020 (Micrometrics), degassing the sample at 200°C for 18 h within the apparatus prior to testing.

The vapor adsorption equilibrium experiments were performed on a VTI-SA vapor sorption analyzer from TA Instruments (New Castel, DE, United States) at temperatures of 25 – 55°C or 25 – 45°C for water and ethanol respectively. The vapor activity was controlled automatically by mixing a saturated vapor feed (using $N_2$ as the carrier gas) with dry $N_2$. The sample "dry mass" was measured under $N_2$ and was at equilibrium before introduction of the vapors to the sample chamber. The isotherms within 0.05 – 0.95 activity were obtained for both ethanol and water.

Using the same instrumentation, vapor adsorption rate experiments were performed at temperature of 25 – 45°C. A large $N_2$ purge flow rate was used to minimize extraneous heat and mass transfer effects.

*5.3. Models and Theory*

Due to dramatic differences in sorbate-sorbent systems, different models are applied to correlate and analyze the sorption isotherms. The Polanyi potential theory is used to fit the water adsorption isotherms while the Langmuir model is used for fitting the ethanol sorption isotherms.

*Polanyi Potential Theory*

In the Polanyi potential theory, the adsorption potential, ε, is defined at the work done by adsorption forces in transferring molecules from the gas phase to the sorbed phase on the adsorbent surface [15]. For one mole of idea gas, ε can be estimated as

$$\varepsilon = \int_{p}^{p_0} V dp = RTln\left(\frac{p_0}{p}\right) \tag{5.1}$$

where $p$ is the vapor pressure and $p_0$ is the saturated vapor pressure. Due to the primarily temperature-independent forces contributing to the adsorption potential, ε is largely a function of the adsorbed sorbate volume (or the mass of the adsorbed phase assuming liquid density for the sorbate) [16]. There for, the adsorption potential can be rewritten as:

$$q = f(\varepsilon) = f\left[RTln\left(\frac{p_0}{p}\right)\right] \tag{5.2}$$

Where $q$ is the adsorbed amount (mmol sorbate/g sorbent or g sorbate/g sorbent). A plot of $q$ vs $RTln(p_0/p)$ gives a unique temperature-independent relation for the fixed sorbate-sorbent system, known as the "characteristic curve". Once the characteristic-curve is obtained, the potential theory can be used to predict an equilibrium isotherm at different temperatures.

*Langmuir Model*

The Langmuir model is expressed as

$$\frac{q}{q_s} = \frac{bp}{1+bp} \tag{5.3}$$

where $q_s$ is the saturation limit and the parameter $b$ is related to the heat of adsorption [17]. Henry's constant, $K=bq_s$, can be obtained by plotting $1/q$ vs $1/p$ and using the linear form of the Langmuir model:

$$\frac{1}{q} = \frac{1}{q_s} + \frac{1}{bq_s}\frac{1}{p} \tag{5.4}$$

The parameter $b$ reflects the degree of adsorption strength of adsorption onto the surface of the adsorbent. Using $b$, the heat of adsorption can be calculated from

$$b = b_o \exp\left(\frac{\Delta H_{ads}}{RT}\right) \tag{5.5}$$

And is equivalent to the isosteric heat of adsorption as long as the saturation limit is independent of temperature.

*Isosteric Heat of Adsorption*

Using the Clausius-Clapeyron equation, the isosteric heat of adsorption, $\Delta H_{iso}$, can be derived as

$$\Delta H_{iso} = RT^2 \left(\frac{\partial lnp}{\partial T}\right)_{\mathcal{T}} \tag{5.6}$$

where $q$ indicates constant equilibrium adsorption quantities. Isosteric heat of adsorption can also be calculated by measuring adsorption isotherms at different temperature and employing the thermodynamic relationship of Equation 5.6. A plot of *ln p* against *1/T* at constant adsorption uptake yields a straight line with a slope of $(\Delta H_{iso}/R)$.

*5.4. Results and Discussion*

*Water Adsorption*

Water vapor isotherms at 35°C for silicalite-1 ($OH^-$) and silicalite-1 ($F^-$) are illustrated in Figure 5.2. The adsorption isotherms at other temperatures (which exhibited similar behavior) can be found in the supplementary information of the *Langmuir* paper [12].

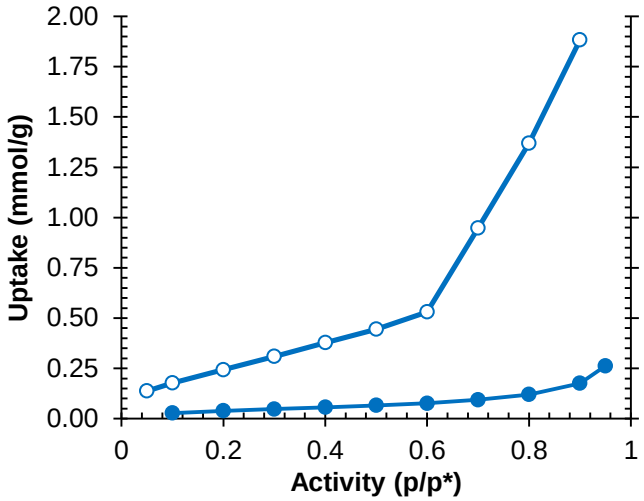


**Figure 5.2.** Water adsorption isotherms for silicalite-1 ($OH^-$), open circles, and silicalite-1 ($F^-$), closed circles, measured at 35°C.

According to BDDT classifications, silicalite-1($OH^-$) exhibits a Type II isotherm, whereas silicalite-1($F^-$) exhibits a Type V isotherm (due to its continued water uptake above saturation pressure [18, 19]. These isotherms are formed due to strong sorbate-sorbate interaction, rather than sorbate-sorbent interactions where the water molecules contact the hydrophobic zeolite framework. These interactions agree well with weak adsorption observed in the low activity regions, indicating the absolute value of adsorption enthalpy for the first layer is likely smaller than the liquefaction enthalpy of water. As adsorption precedes, the adsorbed water molecules act as "seeds" for the adsorption of additional water molecules.

Between the two samples, silicalite-1($F^-$) had the most hydrophobic response, having a water uptake of only 0.263 mmol/g at 35°C and 0.95 activity, accounting for only 12.6% of the

capacity of silicalite-1($OH^-$) under the same conditions (2.08 mmol/g). At a lower activity of 0.05, the same trend is observed, with the water uptake of silicalite-1 ($F^-$) being only 0.024 mmol/g and silicalite-1($OH^-$) having a water uptake of 0.138 mmol/g. The hydrophobicity of silicalite-1($F^-$) can also be demonstrated by determining the initial water cluster size. The water/unit cell ratio ($H_2O$/UC) is determined by extrapolating the first plateau region in the isotherms to an infinitely small vapor pressure (or activity) [20]. As shown in Table 5.I, the initial $H_2O$/UC for the two silicalites is about 0.11 and 0.56 at 35°C for silicalite-1($F^-$) and silicalite-1($OH^-$) respectively.

**Table 5.I.** Initial water cluster size for silicalite-1($F^-$) and silicalite-1($OH^-$) at different temperatures.

| Sorbent | T [°C] | $H_2O$/UC |
|---|---|---|
| Silicalite-1($F^-$) | 25 | 0.12 |
| | 35 | 0.11 |
| | 45 | 0.11 |
| Silicalite-1($OH^-$) | 25 | 0.57 |
| | 35 | 0.56 |
| | 45 | 0.51 |

The distinct difference between the hydrophobicity of the two silicalites is believed to be attributed to the relative number of internal structural silanol defects. Though both have external terminating silanol defects, their impact for the relatively large crystals in this study is expected to be small [21]. The idea hydrophobic silicalite-1($F^-$) can be obtained with fewer internal silanol defects by using fluoride as the mineralizing agent at near neutral conditions. Silicalite-1 prepared by the traditional routes at alkaline conditions with $OH^-$ as the mineralizing agent, however, usually have considerable internal silanol defects created on removal of the charge balancing centers for the template tetraproplyammonium cations (i.e. normally 4 per UC) [10]. In this fluoride route, the $F^-$ offset the template ions in a way that generates few internal defects

[10]. The structural silanol defects can be identified by using nuclear magnetic resonance (NMR). By comparing $^{29}$Si cross polarization magic-angle-spinning (CP-MAS) NMR spectra with its corresponding $^{29}$Si MAS NMR specta, the existence of small amounts of defects can be revealed by an enhanced peak in $^{29}$Si CP-MAS NMR that results from the cross-polarization of Si-OH with $^{1}$H. The fluoride mediated silicalite-1 shows no additional peak in its $^{29}$Si CP-MAS NMR specta, which implies the presence of negligible amounts of silanol defects [8,9]. The spectra of silicalite-1 synthesized by the traditional alkaline condition, however, show extra peaks that are ascribed to the Si-O$^-$ framework defects. While these NMR experiments were not conducted in this study, similar results are expected for the materials used. The increased quantity of polar/hydrophilic silanol defects in silicalite-1(OH$^-$) provide additional water sorption sites within the crystal, attributing to the larger water uptake, when compared to nearly defect free silicalite-1(F$^-$).

The isosteric heats of adsorption of water in silicalite-1(F$^-$) and silicalite-1(OH), along with H-ZSM-5 Si/Al:140 for comparison, are summarized in Figure 5.3.

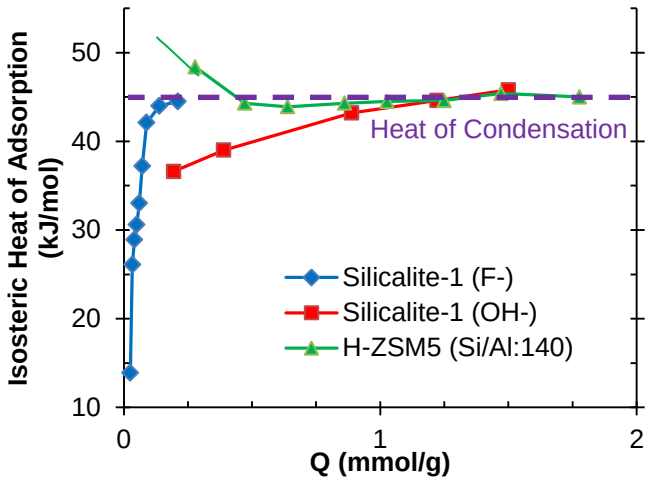


**Figure 5.3.** Isosteric heats of adsorption for water adsorption in silicalite-1(F$^-$) silicalite-1(OH$^-$), and H-ZSM-5 with a Si/Al ratio of 140. Each data point represents the average of at least two measurements.

The results indicate that for both silicalite-1($F^-$) and silicalite-1($OH^-$), the isosteric heats of adsorption increase with increased adsorption amounts, reflecting their hydrophobic nature. The low heats of adsorption silicalite-1($F^-$) imply that adsorption of water within near defect-free structure is only marginally thermodynamically spontanius. The adsorption of water at low activities is attributed to the physisorption of water to the hydrophobic framework, while at higher activities, the initially physisorbed water act as seeds for subsequent water clustering. The stronger water-water interactions under these conditions attribute to the higher isosteric heats of adsorption and water adsorption continues until the zeolite framework is homogenously covered with water. The isosteric heats of adsorption of silicalite-1($OH^-$) exhibits a similar trend, but a higher initial heat of adsorption and less-steep slope are observed, likely do the presence of additional silanol defects which act as weak hydrophilic sites. H-ZSM-5, however, exhibits the opposite trend from both silicalite synthesis methods, with higher heats of adsorption at low water uptake, decreasing to the heat of condensation at higher uptakes. This trend is the result of highly favorable water adsorption on the hydrophilic Al sites within the ZSM-5 structure.

The water vapor uptake for both silicalites at all temperatures and activities tested are plotted as a function of the adsorption potential in the paper presented in *Langmuir* [12]. The adsorption data for each sorbent conform to one respective characteristic curve, indicating the potential theory model reasonably describes the water-MFI sorption system in this study. These models can easily be used to predict the adsorption uptake at any activity and temperature by simply calculating the corresponding adsorption potential.

*Ethanol Adsorption*

The ethanol vapor adsorption isotherms for silicalite-1($OH^-$) and silicalite-1($F^-$) at 35°C are shown in Figure 5.4. The adsorption isotherms at other temperatures can be found in the supplementary information of the *Langmuir* paper [12]. Both silicalites reached near saturation adsorption at pressures below the saturation pressure, indicating an overall organophilic nature. Unlike the water uptake in these two materials, the ethanol uptake is practically identical for both synthesis routs. The weakly hydrophilic structural defects in silicalite-1($OH^-$) seem to have no significant effect on the ethanol loadings.

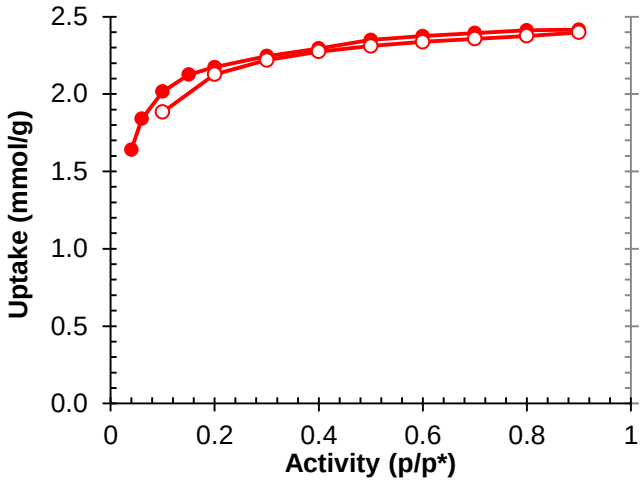


**Figure 5.4.** Ethanol adsorption isotherms for silicalite-1($OH^-$), open circles, and silicalite-1($F^-$), closed circles, at 35°C.

The isotherms for both ethanol isotherms are of the Type-I form, which can be described by the Langmuir model. Table 5.II lists the Langmuir model parameters for ethanol adsorption in silicalite-1($F^-$) and silicalite-1($OH^-$). The saturation limit values, $q_s$, are between 11.3-11.7% (sorbent wt%) and decrease slighty with increasing temperature, as is expected. For microporus materials, the saturation limit in Type-I isotherms reflects the micropore filling, where the total volume of micropore filling corresponds to the quantity adsorbed. There for the saturation limit is expected to be temperature independent as long as the pore volume and zeolite structure do not

change. The slight decrease in this value is likely due to the greater expansion coefficient of ethanol than the zeolite framework [22]. Using equation 5.6, the heats of adsorption of ethanol in silicalite-1($F^-$) and silicalite-1($OH^-$) were determined to be 35.8 and 36.5 kJ/mol, respectively.

**Table 5.II.** Langmuir parameters for ethanol adsorption in silicalite-1($F^-$) and silicalite-1($OH^-$). Error estimates indicate the quality of the model fits to the experimental data.

| Sorbent | T [°C] | $q_s$ (%) | $bq_s$ ($Pa^{-1}$) | $R^2$ |
|---|---|---|---|---|
| Silicalite-1($F^-$) | 25 | 11.68 ± 0.06 | 0.0417 ± 0.0015 | 0.992 |
| | 35 | 11.55 ± 0.02 | 0.0254 ± 0.0003 | 0.999 |
| | 45 | 11.24 ± 0.03 | 0.0184 ± 0.0004 | 0.997 |
| Silicalite-1($OH^-$) | 25 | 11.62 ± 0.07 | 0.0463 ± 0.0023 | 0.985 |
| | 35 | 11.32 ± 0.03 | 0.0267 ± 0.0005 | 0.998 |
| | 45 | 11.41 ± 0.03 | 0.0178 ± 0.0004 | 0.997 |

*Ideal Ethanol/Water Sorption Selectivity*

The low water uptakes and the organophilic nature of silicalite-1($OH^-$) and silicalite-1($F^-$) reported here indicate that both materials have the potential to be applied for ethanol removal from water processes. The ideal vapor phase selectivity ethanol/water sorption selectivity, $\alpha$, is defined as

$$\alpha_{E/W} = \frac{C_{EtOH,sorbed}/C_{water,sorbed}}{C_{EtOH,vapor}/C_{water,vapor}} \tag{5.7}$$

where C is the concentration of ethanol or water in the vapor or adsorbed phase, and can be estimated using the pure-vapor adsorption isotherms. Raoult's law and Henry's law are used to estimate the vapor pressures of water and ethanol respectively. The estimated ideal sorption selectivity for ethanol concentration range of 1-5 mol% in water are summarized in Figure 5.5 for both materials.

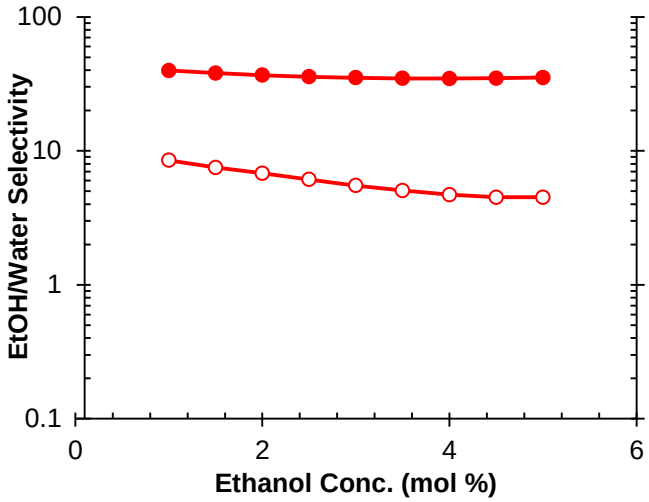


**Figure 5.5**. Ideal ethanol/water sorption selectivity at 35°C for silicalite-1($OH^-$), open circles, and silicalite-1($F^-$), closed circles.

Compared to silicalite-1($OH^-$), as well as other MFI-type zeolites, silicalite-1($F^-$) demonstrates superior ethanol removal capability and is of an order of magnitude higher, increasing from 36 to 53 when ethanol concentration decreases from 5 to 1 mol% (balance water). Silicalite-1($OH^-$) show sorption selectivites of 4.5-8.3 for the same liquid concentration range of ethanol in water.

While binary vapor sorption is beyond the scope of this work, competitive ethanol/water sorption selectivity is expected to be lower than pure vapor results for both silicalite-1($OH^-$) and silicalite-1($F^-$). It is hypothesized that the adsorbed ethanol and water molecules will act as "seeds" for additional water sorption due to the exposed –OH tails. However, this effect is expected to be less for silicalite-1($F^-$) due to the reduced quantity of defects sites for initial water adsorption.

*Diffusion of Ethanol and Water in Silicalite-1($F^-$)*

As shown in Figure 5.6, the transient uptake curves for ethanol and water adsorption exhibit typical behavior expected for a diffusion controlled process (linear with $\sqrt{t}$ in the initial region) and have been interpreted in terms of the usual diffusion model. While additional mass transfer resistance at the crystal surface cannot explicitly be excluded, the good fit of the model indicates that the mass transfer rate must be controlled primarily by intra-crystalline diffusion.

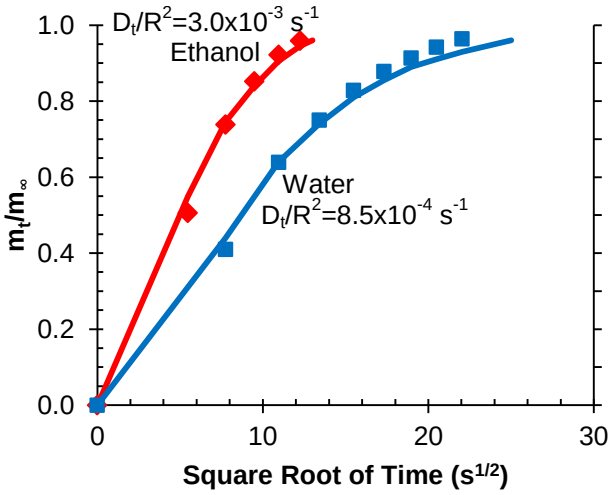


**Figure 5.6.** Representative uptake curves for water (blue) and ethanol (red) in silicalite-1($F^-$) at 35°C and activity =0.3, showing the fit of the experimental data to the theoretical curves calculated from Equation 5.8.

In an ideal silicalite crystal (with MFI-type morphology), the strait and sinusoidal channels are oriented perpendicularly in the *x* and *y* directions (the sorter crystal dimensions). However, in the real crystals, sub-structure twinning disrupts the channel paths, resulting in channels in the *x* and *y* directions being comprised of both strait and sinusoidal segments [23, 24]. As a result, the diffusion in the *x* and *y* directions are essentially the same. In the *z* direction there is no distict channel, so diffusing molecules have to jump between strait and sinusoidal channels. As a result, uptake primarily occurs in the *x* and *y* directions, with minimal uptake

contribution from the ends of the crystal. The model that best captures this system represents the crystals as infinite cylinders have the same external area/volume ratio as the actual crystals. From the average dimensions of the crystals used in this study, 70 x 30 x 15 μm, an equivalent cylinder radius, *R*, of 10 μm is assumed for the model.

Given by Crank, the transient diffusion, giving the fractional uptake as a function of time, for an infinite cylinder (radius *R*) subject to a step change in sorbate concentration at the external surface can be described by

$$\frac{m_t}{m_\infty} = 1 - 4\sum_{n=1}^{\infty}\frac{1}{\alpha_n^2}\cdot\exp\left(-\frac{Dt\alpha_n^2}{R^2}\right) \qquad J(\alpha_n) = 0 \tag{5.8}$$

where $J_0$ is the zero order Bessel function of the first kind and $\alpha_n$ is the positive root of $J_0(\alpha_n)=0$. The time constant ($D_t/R^2$), and thus the intra-crystalline diffusivity, was obtained by fitting the experimental uptake curves to this expression. Note that an "interval" diffusivity, over some limited activity range, is measured step-by-step with increasing activity rathat than "integral" diffusivity (from 0 to some final activity).

At 35°C and an activity of 0.3, the measured transient uptake of water into silicalite-1($F^-$) is significantly slower than that of ethanol ($D_t$ values of $8.5\text{x}10^{-10}$ $cm^2/s$ and $2.6\text{x}10^{-9}$ for water and ethanol respectively). As activity increased, higher uptake rates for both ethanol and water are observed, as seen in Figure 5.7. The faster diffusion of ethanol in comparison to water, kinetic diameters of 0.446 nm and 0.265 nm respectively, seems surprising, but this difference arises primarily from the difference in shape of the equilibrium isotherms. The Fickian diffusion model assumes a concentration gradient driving force for molecular transport, but the fundamental driving force is in fact a chemical potential gradient. Using the relationship between concentration based (Fickan) diffusion, $D_{t,}$ and the thermodynamically corrected diffusivity, $D_0$:

$$D_t = D_0 \frac{\partial lnp}{\partial lnq} \tag{5.9}$$

(where $\frac{\partial lnp}{\partial lnq}$ is the gradient of the equilibrium isotherm in logarithmic coordinates) the measured diffusivities can be adjusted to accurately reflect the mobility of each species in silicalite-1($F^-$) [25, 26]. For equilibrium isotherms with a favorable Type-I isotherm (like ethanol), $\frac{\partial lnp}{\partial lnq}$ increases with increasing concentration, approaching very large values in the saturation region. The thermodynamically corrected values, shown in Figure 5.7, are significantly lower than the corrected values for water, which only changed slightly, and more accurately reflect the relative mobility of each molecule. From these results, it is evident that the high transport diffusivity of ethanol is largely due to the highly favorable equilibrium isotherm.

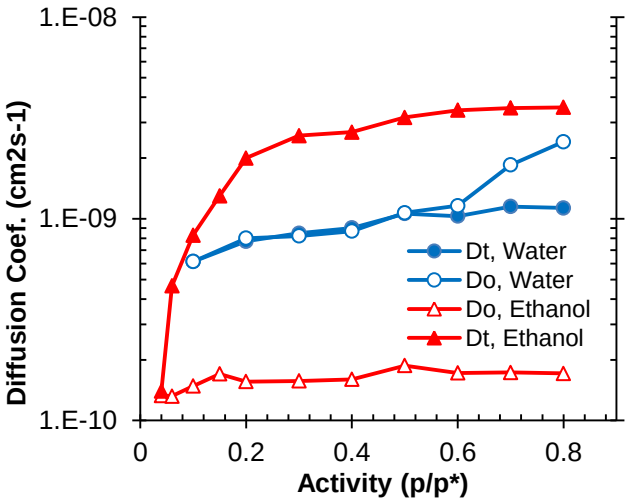


**Figure 5.7.** Concentration dependence of $D_t$ and $D_0$ for water and ethanol diffusion in silicalite-1($F^-$) at 35°C.

These results are confirmed by the activation energies, calculated in the typical way using the Arrhenius expression:

$$D_0 = D_0' \exp\left(-\frac{E_d}{RT}\right) \tag{5.10}$$

The activation energies, calculated using a 25 - 45°C temperature range, are shown in Figure 5.8 for 0.05 – 0.7 activity. The lower values for water, as compared to ethanol, reflect the higher intrinsic mobility of the smaller molecule.

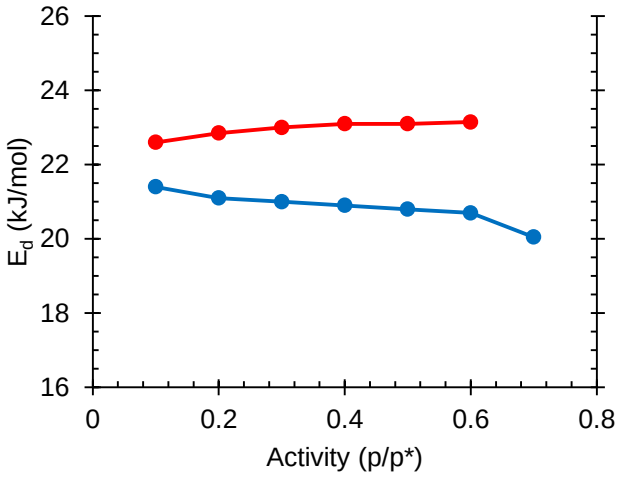


**Figure 5.8**. Activation energy $E_d$ for water (blue) and ethanol (red) as a function of sorbate activity.

*Permeability and perm-selectivity*

Using the equilibrium (adsorption isotherms) and kinetic (diffusion) obtained in this study, the permeability and perm-selectivity for ethanol and water in silicalite-1($F^-$) can be calculated using the definition of permeability:

$$P_i = D_i \times S_i \tag{5.11}$$

where $P_i$, $D_i$, and $S_i$ are the permeability, transport diffusivity $D_t$, and sorption coeficient of species $i$, respectively. The sorption coefficient is determined by normalizing the equilibrium uptake ($\Delta q_i$) by the pressure driving force ($\Delta p_i$):

$$S_i = \frac{\Delta q_i}{\Delta p_i} = \frac{q_i}{p_i} \tag{5.12}$$

where $q_i$ and $p_i$ are the sorption amount and vapor pressure of species $i$, respectively. Figure 5.9 illustrates the ethanol and water permeability in silicalite-1($F^-$) at 35°C estimated using the uptake rates and adsorption isotherms.

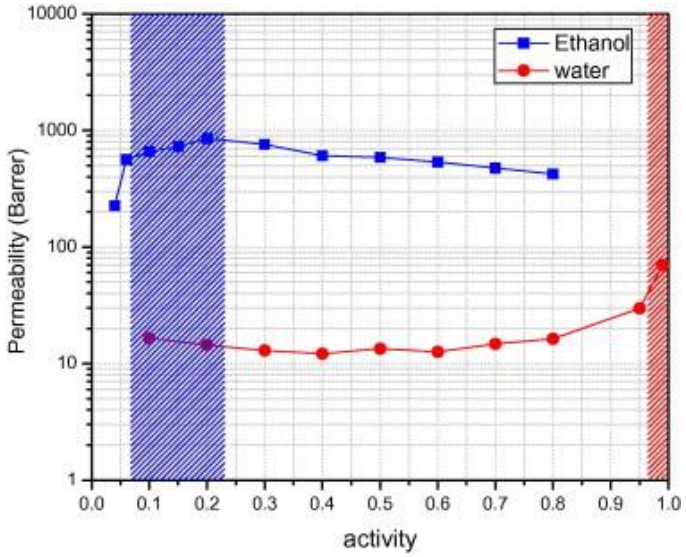


**Figure 5.9.** Estimated ethanol and water permeability in silicalite-1($F^-$) at 35°C. The hashed regions indicate typical vapor activities for ethanol (1-5 mol%) and water (95-99 mol%) liquid streams.

The predicted water permeability in silicalite-1($F^-$) is extremely low, ranging only from 10.5 – 70 Barrer from 0.1 to unit activity, while the predicted ethanol permeability is almost a full order of magnitude higher, ranging from 110 – 800 Barrers from 0.045 – 0.8 activity. While the low water permeability can be attributed to the extremely low concentration of internal silanol defects in the fluoride mediated silicalite-1, the ethanol permeabilities are consistent with those reported for other silicalite-1 synthesis routes under similar conditions [27 -31].

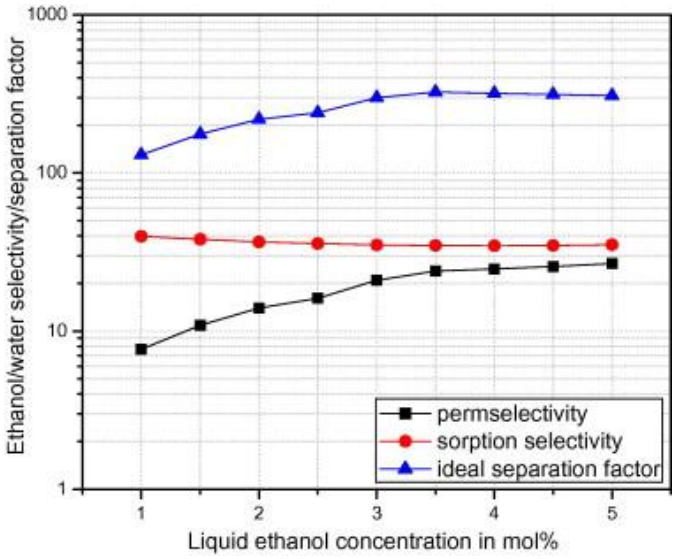


**Figure 5.10**. Ethanol/water permelectivity, sorption selectivity, and ideal separation factor at 35°C for 1-5 mol% ethanol (balance water).

The vapor phase idea ethanol/water perm-selectivity, sorption selectivity, and separation factor are reported in Figure 5.10 for feeds with 1 – 5 mol% ethanol concentrations. For pervaporation membranes, the ethanol/water separation factor, $\beta_{e/w}$, can be defined as

$$\beta_{e/w} = \frac{y_e/y_w}{x_e/x_w} = \alpha_{e/w} \cdot \left(\frac{p_e^*}{p_w^*}\right)\left(\frac{\gamma_e}{\gamma_w}\right) \tag{5.13}$$

where $y_e/y_w$ is the mole fraction of ethanol/water vapor in the permeate stream, $x_e/x_w$ is the mole fraction of ethanol/water in the feed liquid, $\alpha_{e/w}$ is the perm-selectivity, and $\left(\frac{p_e^*}{p_w^*}\right)\left(\frac{\gamma_e}{\gamma_w}\right)$ is the volatility factor. As reported earlier, the sorption selectivity ranges from 35 to 40 for 1 – 5 mol% ethanol, while the ethanol perm-selectivity lies between 7 and 27 over the same ethanol concentration. The perm-selectivity is lower than the sorption selectivity due to the unfavorable influence of diffusion selectivity at low ethanol concentrations. As ethanol concentration increases, the influence of diffusion selectivity becomes less significant, and perm-selectivity approaches sorption selectivity. The separation factor, on the other hand, are estimated to be 130 – 310 by the pure vapor sorption and diffusion tests. These factors are largely enhance mainly

due to the large volatility factor for ethanol and water. Since ethanol has larger saturation pressures and activity coefficients that water in the area of interest (1 – 5 mol% ethanol), the separations factors are an order of magnitude larger that the perm-selectivity. While it is likely competitive sorption will results in lower separation factors for binary ethanol-water mixture tests, the predicted separation factors for silicalite-1($F^-$) are significantly larger than what is reported in the literature for silicalite-1 synthesized by other routes ($\beta_{e/w}$: 10 – 64) [27-31]. It is clear that fluoride mediated silicalite-1 is promising for ethanol removal from dilute aqueous mixtures, largely in part to its significantly depressed water adsorption and uptake rates.

*5.4. Conclusions*

Water and ethanol vapor adsorption in silicalite-1($OH^-$) and silicalite-1($F^-$) revealed the significant impact the relative number of internal silanol defects has on the hydrophobicity of pure silica MFI-type zeolites. While there was no significant difference in the ethanol isotherms for both synthesis routes, near defect-free silicalite-1($F^-$) had a water uptake of only 0.176 mmol/g-sorbent at 35°c and unit activity, a full order of magnitude lower than the water uptake up silicalite-1($OH^-$) under the same conditions. Using the measured isotherms, the ethanol/water sorption selectivity ranging from 36 – 53 was estimated for 1 – 5 mol% ethanol concentrations. Additionally, measured uptake rates of ethanol and water in silicalite-1($F^-$) revealed transport diffusivities similar to those reported in the literature.

From the diffusivity data together with the equilibrium isotherm data, the permeability and perm-selectivity of ethanol and water in a silicalite-1($F^-$) membrane were approximated. Based on such estimates, a comparison of fluoride mediated silicalite-1 and the standard

silicalite-1 synthesized in alkaline conditions suggest that silicalite-1($F^-$) should have a considerable advantage for use in extraction of ethanol from dilute aqueous solutions.

**REFERENCES**


1. J Caro, M. Noack, P. Kolsch, R. Schafer. *Microporous Mesoporous Mater*., 38 (2000), pp. 3–24.
2. M. Kanezashi, J. O'Brien, Y.S. Lin. *J. Membr. Sci.*, 286 (2006), pp. 213–222
3. J. O'Brien-Abraham, M. Kanezashi, Y.S. Lin. *Microporous Mesoporous Mater*., 105 (2007), pp. 140–148
4. NY Chen. Hydrophobic properties of zeolites. *J. Phys. Chem.* 1976, 80 (1), 60−64.
5. J. Caro, M. Bulow, J. Richtermendau, J. Karger, M. Hunger, D. Freude, L.V.C. Rees. *J. Chem. Soc.-Faraday Trans. I*, 83 (1987), p. 1843.
6. JM Chezeau et al.. Influence of synthesis conditions and postsynthesis treatments on the nature and quantity of structural defects in highly siliceous MFI zeolites-A highresolution solid-state Si-29 NMR-study. *Zeolites* 1991, 11 (6), 598−606.
7. JM Chezeau, et al. Highresolution solid-state Si-29 and C-13 NMR on highly siliceous MFItype zeolites synthesized in nonalkaline fluoride medium. *Zeolites.* 1989, 9 (1), 78−80.
8. SA Axon and J Klinowski. Synthesis and characterization of defect-free crystals of MFI-type zeolites. *Appl. Catal., A* 1992, 81 (1),27−34.
9. SA Axon, and J Klinowski. Nuclear-magnetic-resonance studies of the synthesis of zeolite ZSM-5 by the fluoride method. *Appl. Catal*., A 1994, 111 (1), 29−39
10. MA Camblor, LA Villaescusa, and JM Diaz-Cabanas. Synthesis of all-silica and high-silica molecular sieves in fluoride media. *Top. Catal*. 1999, 9 (1−2), 59−76.
11. M.L. Gualtieri, A.F. Gualtieri, M. Prudenziati. *Microporous Mesoporous Mater*., 111 (2008), pp. 604–611.
12. K. Zhang, R.P. Lively, J.D. Noel, M.E. Dose, B.A. McCool, R.R. Chance, W.J. Koros. *Langmuir*, 28 (2012), pp. 8664–8673.
13. K Zhang, et al. *Microporous and Mesoporous Materials*. 170 (2013) pp 259 – 265.
14. Fyfe, C. A.; Brouwer, D. H.; Lewis, A. R.; Chezeau, J. M.. Location of the fluoride ion in tetrapropylammonium fluoride silicalite-1 determined by H-1/F-19/Si-29 triple resonance

CP, REDOR, and TEDOR NMR experiments. J. Am. Chem. Soc. 2001, 123 (28), 6882−6891.

15. Yang, R. T. Gas separation by adsorption processes; Imperial College Press: London, 1987; Vol. 1.
16. Chang, H.; Yuan, X. G.; Tian, H.; Zeng, A. W. Experimental investigation and modeling of adsorption of water and ethanol on cornmeal in an ethanol-water binary vapor system. Chem. Eng. Technol. 2006, 29 (4), 454−461.
17. Ruthven, D. M.; Kaul, B. K. Adsorption of aromatic hydrocarbons in NaX zeolite. 1. Equilibrium. Ind. Eng. Chem. Res.1993, 32 (9), 2047−2052.
18. Eroshenko, V.; Regis, R. C.; Soulard, M.; Patarin, J. Energetics: A new field of applications for hydrophobic zeolites. J. Am. Chem. Soc. 2001, 123 (33), 8129−8130.
19. Desbiens, N.; Boutin, A.; Demachy, I. Water condensation in hydrophobic silicalite-1 zeolite: A molecular simulation study. J. Phys. Chem. B 2005, 109 (50), 24071−24076
20. Olson, D. H.; Haag, W. O.; Borghard, W. S. Use of water as a probe of zeolitic properties: interaction of water with HZSM-5. Microporous Mesoporous Mater. 2000, 35−6, 435−446.
21. Cheng, C.-H.; Bae, T.-H.; McCool, B. A.; Chance, R. R.; Nair,S.; Jones, C. W. Functionalization of the internal surface of pure-silica MFI zeolite with aliphatic alcohols. J. Phys. Chem. C 2008, 112 (10), 3543−3551.
22. Cavalcante, C. L.; Ruthven, D. M. Adsorption of branched and cyclic paraffins in silicalite. 1. Equilibrium. Ind. Eng. Chem. Res. 1995, 34 (1), 177−184.
23. L. Karwacki, M.H.F. Kox, D.A.M. de Winter, M.R. Drury, J.D. Meeldijk, E. Stavitski, W. Schmidt, M. Mertens, P. Cubillas, N. John, A. Chan, N. Kahn, S.R. Bare, M. Anderson, J. Kornatowski, B.M. Weckhuysen Nat. Mater., 8 (2009), pp. 959–965.
24. M.B.J. Roeffaers, R. Ameloot, A.J. Bons, W. Mortier, G. De Cremer, R. de Kloe, J. Hofkens, D.E. De Vos, B.F. Sels J. Am. Chem. Soc., 130 (2008), p. 13516.
25. N.Y. Chen, T.F. Degnan, C.M. Smith. Molecular Transport and Reaction in Zeolites: Design and Application of Shape Selective Catalysis. John Wiley and Sons (1994).
26. J. Kärger, D.M. Ruthven Diffusion in Zeolites and Other Microporous Solids Wiley (1992).
27. B. Soydas, O. Dede, A. Culfaz, H. Kalipcilar Microporous Mesoporous Mater., 127 (2010), pp. 96–103.

28. V.A. Tuan, S.G. Li, J.L. Falconer, R.D. Noble. J. Membr. Sci., 196 (2002), pp. 111–123.
29. M. Nomura, T. Yamaguchi, S. Nakao. J. Membr. Sci., 144 (1998), pp. 161–171.
30. M. Nomura, T. Yamaguchi, S. Nakao. J. Membr. Sci., 187 (2001), pp. 203–212.
31. V. Sebastian, R. Mallada, J. Coronas, A. Julbe, R.A. Terpstra, R.W.J. Dirrix. J. Membr. Sci., 355 (2010), pp. 28–35.

# CHAPTER 6

# MIXED MATRIX MEMBRANES FOR ETHANOL-WATER PERVAPORATION

## *6.1. Introduction*

Membrane based separation processes are emerging as attractive options over the more commonly used – and more energy intensive – industrial separations. In particular, the removal of ethanol from dilute aqueous streams using ethanol selective membranes would be of great benefit due to the large energy penalty associated with the distillation process currently in use for this process. The standard hydrophobic membranes used for ethanol removal from aqueous solutions are made of polydimethylsiloxane (PDMS), a type of silicone rubber. Unfortunately, the ethanol water perm-selectivity of PDMS is only about 0.70, meaning it is actually selective to water [1]. In order to improve this performance, mixed matrix membranes are often prepared with hydrophobic fillers to boost the hydrophobicity, and thus the selectivity, of PDMS. Composite membranes containing different weight loading of ZSM-5 with high Si/Al ratios and silicalite-1($OH^-$) have been thoroughly studied with reasonable performances achieved for high weight loadings (< 50 wt%). As discussed in the previous two chapters, the two additional materials (ZIF-71 and silicalite-1($F^-$) have been studied and show water uptakes significantly less than that of silicalite-1($OH^-$). In this chapter, the pervaporation performance of mixed matrix membranes containing ZIF-71 and silicalite-1($F^-$) have been investigated and compared to that of the heavily studied ZSM-5 and silicalite-1($OH^-$) PDMS composite membranes.

*6.2. Materials and Methods*

*Filler Synthesis*

ZIF-71 was synthesized using the methanol derived approach decribed previously in Chapter 4 and in *Chemical Communications* [2]. Silicalite-1($F^-$) was synthesized using the same procedure described in Chapter 5, with the exception of dispersing 50 mg of "seeds" (ball milled silicalite-1($F^-$) synthesized normally) and reducing the synthesis time at 180°C from 14 days to 4 days. The same washing and calcination procedures were used. The resulting crystals had a platelet (verses a coffin) morphology with dimensions of 3.6 x 0.60 x 13.5 μm (Figure 6.1), making them more suited for incorporating into a mixed matrix membrane. Silicalite-1($OH^-$) with a particle size of 1 – 3 μm was purchased from Sigma Aldrich.

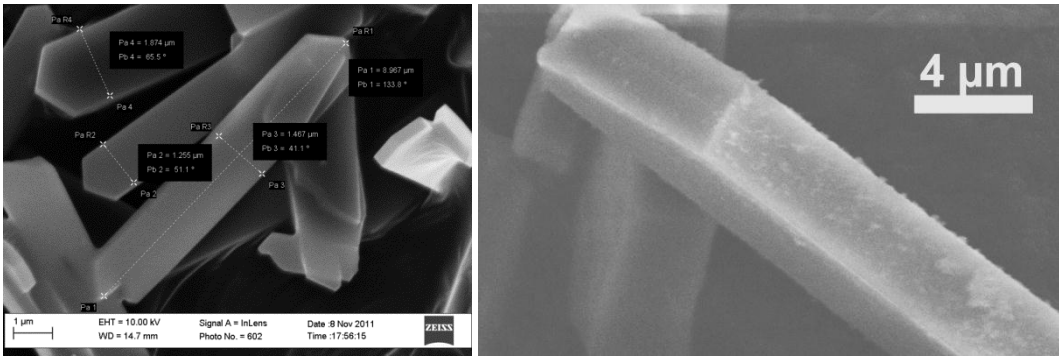


**Figure 6.1.** SEM image of platelet silicalite-1($F^-$).

*Mixed Matrix Membrane Casting*

Prior to forming the casing dope for any of the membranes, each of the fillers were dried at 110°C for a minimum of 12 h to remove any adsorbed water. Silicalite-1($F^-$) and silicalite-1($OH^-$) mixed matrix membranes were prepared using the same method. The mass of the silicalite-1 necessary to form the desired weight loading was added to a 15 mL scintillation vial and dispersed in 7.0 g of toluene (anhydrous, Sigma Aldrich) using three 60 s bursts from a sonication horn (1000W max horn, Dukane, Leesburg, VA) with vigorous vortex mixing (Digital

Vortex Mixer 120V, Fisher Scientific) between bursts. The PDMS base (2.00 g, SYLGARD 184 Silicon Elastomer Base, Dow Chemicals) was then added to the dispersion, followed by two additional sonication/vortex cycles. While stirring vigorously with a stir bar, a $N_2$ purge was used to remove the excess solvent and increase the viscosity of the dope. When the dope contained < 20 wt% solvent, the $N_2$ purge was stopped, and 0.200 g of PDMS curing agent (SYLGARD 184 Silicon Elastomer Curing Agent) was added, using vigorous vortex mixing to disperse thoroughly. Films were then immediately cast using a 4 mil casting knife in a $N_2$ purged, toluene saturated glove bag on a BYTAC® coated glass plate. After standing for 18hrs, the film, adhered to the plate, was removed and transferred to a 100°C oven for a minimum 6 h to cross link to form a sturdy film. The film was them removed from the plate and transferred to a 110°C vacuum oven for 24 h to remove any remaining solvent. Pure PDMS films were made to use as a standard by combining the PDMS base and curing agent in a 10:1 ratio with-out any solvent. After casting on a BYTEC® coated glass plate, the pure PDMS films were cross linked and dried using the same conditions as the mixed matrix membranes.

A similar method was attempted for forming ZIF-71/PDMS mixed matrix membranes. As with the ZIF-8 in 6FDA-DAM:DABA(4:1), it is believed the thermal crosslinking step, required for the addition cure SYLGARD 184, induced an undesired reaction between polymer and the catalytic zinc in the ZIF-71. This resulted in films that either did not "set" or formed films with poor mechanical properties that often tore upon removal from the casting plate. To avoid heating the ZIF-71 and PDMS when combined prior to cross linking, a "condensation cure" PDMS was using the place of SYLGARD 184 [3]. To form the dope, the mass necessary to make the desired weight loading was dispersed in 4.00 g of filtered, anhydrous heptane using three 60 s bursts from a sonication horn with 90 s of vigorous vortex mixing between bursts.

After the dispersion returned to room temperature, being sure to keep the mixture moving to prevent agglomeration, 0.50 g of silanol terminated polydimethylsiloxane (Gelest DMS-S45, 110,000 g/mol) was dissolved in the mixture and followed by two sonication-vortex cycles. One drop each (~0.02 g/drop) of titanium 2-ethylhexoxide (Gelest AKT867) and di-n-butyldiacetoxytin tech-95 (Gelest SND3160) were added along with 0.10 g of tetraethyl orthosilicate (TEOS, Sigma Aldrich), using 90 s of vortex mixing to thoroughly combine. The solution was then cast into a Teflon dish (9 cm diameter) in a $N_2$ purged glove back at 60% relative humidity. Due to the cross linking being catalyzed by the presence of water, extra care was taken to ensure the casting mixture remained anhydrous throughout the process. After 4 h, the film was removed from the glove bag and soaked with isopropyl alcohol in a sonication bath for 12 h to remove the catalyst and undesired byproducts from the film. The film dried in a vacuum oven at 110ºC overnight prior testing.

*Pervaporation*

The pervaporation system shown in Figure 6.2 was used to test the ZIF-71, silicalite-1($F^-$), and silicalite-1($OH^-$) PDMS composite membranes. The custom built batch pervaperation cell has a 50 mL feed with a Teflon magnetic stir bar to prevent concentration polarization at the membrane surface. The active area of the membrane (3.93 $cm^2$) is supported by a highly porous stainless steel disk and sealed from the environment and the feed by two gaskets (Figure 6.2). To run a test, the membrane is sealed directly in the cell (without masking) using 15 ft-lbs of torque. After filling the upstream with the desired feed solution and pulling vacuum on the downstream overnight, the system is heated to 50ºC for two hours prior to collecting a sample. After a

measurable sample is collected using the liquid nitrogen trap, the permeate and feed ethanol concentrations are measured using a refractometer.

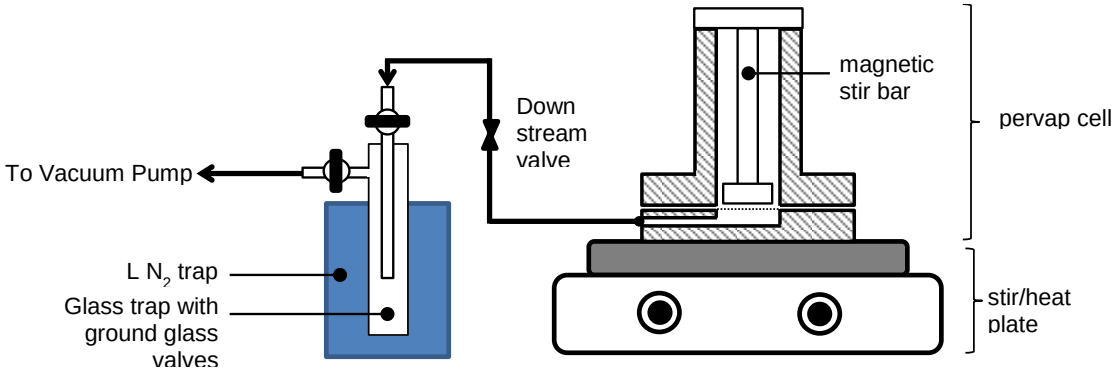


**Figure 6.2**. Top: Pervaporation set up, showing the custom built pervaporation cell and glass trap with ground glass values.

The permeability of ethanol and water are calculated using the definition of a Barrer:

$$1\ Barrer = 10^{-10}\ \frac{(cm^3 STP)\cdot cm}{s\cdot cmHg\cdot cm^2} \tag{6.1}$$

such that:

$$P_i = 10^{10}\cdot\frac{x_i\cdot m\cdot \ell}{\Delta t\cdot MW_i\cdot y_i p_i^*\cdot A}\cdot\left(\frac{22400 cm^3 STP}{mol}\right) \tag{6.2}$$

where $m$ is the sample mass, $\ell$ is the membrane thickness (cm), $A$ is the active membrane area, $\Delta t$ is the sample collection time, and for species $i$, $x_i$ is the mass fraction in the sample, $MW_i$ is the molecular weight (g/mol), $y_i$ is the mole fraction in the feed, and $p_i^*$ is the saturation vapor pressure at 50°C.

*6.3. Results and Discussion*

Membranes containing 5 wt% silicalite-1($F^-$), 20 wt% silicalite-1 ($F^-$), 40 wt% silicalite-1($OH^-$), and 50 wt% ZIF-71 were prepared in the method described above. As shown in Figure 6.3, all of the mixed matrix membranes show good filler adhesion to the polymer matrix with

minimal particle agglomerations. These characteristics are necessary for ideal polymer performance. One clear advantage of using silicalite-1($F^-$) over silicalite-1(OH-) is the effective surface area covered by a single crystal. Due to the platelet morphology, a low weight loading silicalite-1($F^-$) will be able to cover a larger area than an equivalent loading of the spherical silicalite-1($OH^-$). By using a high viscosity and knife casting, alignment of the platelets is shown to be feasible by Figure 6.3a, where the platelet has been aligned perpendicular to the diffusion direction.

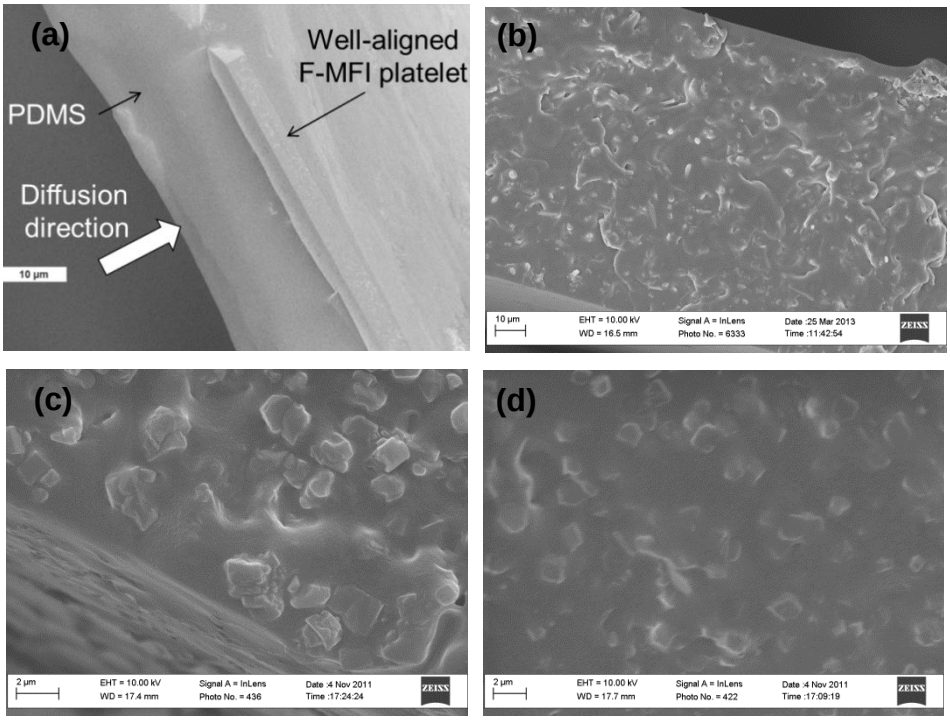


**Figure 6.3.** SEM images of the PDMS mixed matrix membranes used in this study. All films showed both good filler adhesion in the PDMS matrix with minimal agglomeration. (a) 5 wt% Silicalite-1($F^-$), (b) 20 wt% Silcalite-1($F^-$), (c) 40 wt% Silicalite-1($OH^-$), (d) 50 wt% ZIF-71.

Historically, the separation factor and flux are used to report the performance of pervaporation membranes. However, due to being less sensitive to operating conditions,

selectivity is the preferred parameter for comparing membrane performance. The permeability of ethanol and water though the tested membranes along with the ethanol/water selectivity and separation factors are listed in Table 6.I, for 50ºC feeds with 3 wt% ethanol. Figure 6.4 compares the ethanol permeability to the ethanol/water selectivity of the film. Pure PDMS was found to have an ethanol permeability of 23600 Barrers a selectivity of 0.707, agreeing well with previously reported values [1]. Of the tested mixed matrix membranes, the 50 wt% ZIF-71 composite membrane was found to have the largest ethanol permeability, over 2.8 time that of pure PDMS, and largest ethanol water selectivity ($\alpha_{E/W}$ : 1.19).

**Table 6.I**. Pervaporation results at 50°C with a 3 wt% ethanol feed.

| PDMS type | Filler | Loading (wt%) | $P_{EtOH}$ (Barrer) | $P_{water}$ (Barrer) | $\alpha_{E/W}$ | $\beta_{E/W}$ |
|---|---|---|---|---|---|---|
| SYLGARD 184 | -- | 0 | 23600 ± 1690 | 33500 ± 2000 | 0.707 ± 0.05 | 6.86 ± 0.44 |
| SYLGARD 184 | Silcialite-1 ($F^-$) | 5 | 28100 ± 1300 | 37400 ± 1900 | 0.751 ± 0.02 | 7.35 ± 0.15 |
| SYLGARD 184 | Silcialite-1 ($F^-$) | 20 | 27900 ± 1800 | 34100 ± 1100 | 0.821 ± 0.08 | 7.92 ± 0.81 |
| SYLGARD 184 | Silcialite-1 ($OH^-$) | 40 | 28100 ± 3000 | 36100 ± 1500 | 0.78 ± 0.09 | 7.53 ± 0.89 |
| Cond. Cure | ZIF-71 | 50 | 91300 ± 4300 | 76400 ± 869.3 | 1.19 ± 0.04 | 11.7 ± 0.42 |

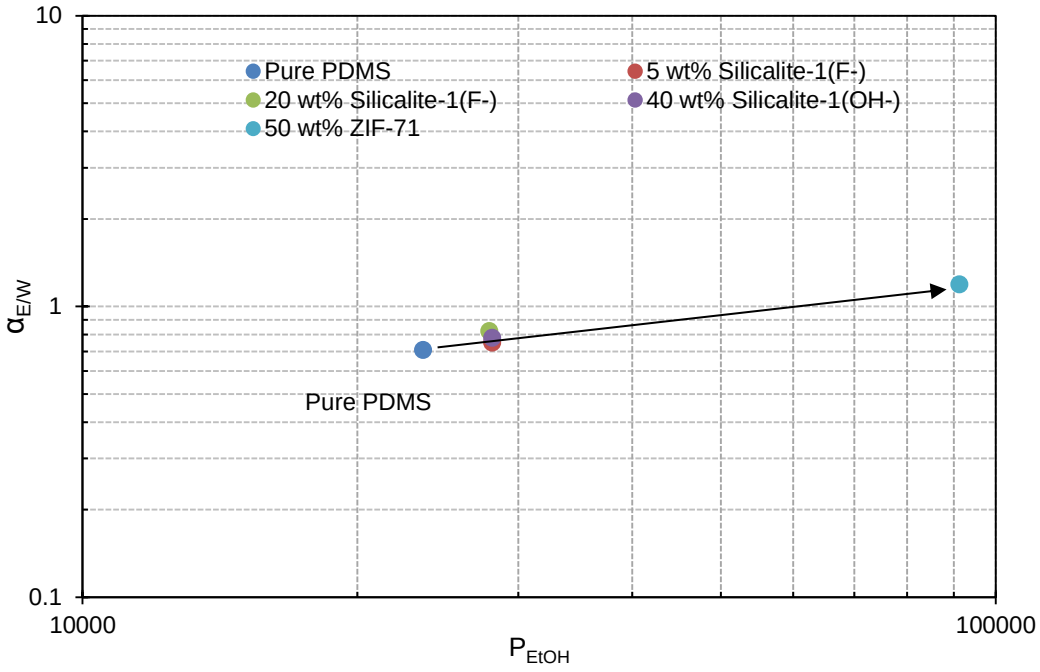


**Figure 6.4**. Pervaporation results at 50°C for 3 wt% ethanol feed, showing the increase in permeability for various filler weight loadings.

To compare performance of the films with different filler weight loadings, the percent increase in ethanol permeability and ethanol/water selectivity were normalized by the volume percent loading of the filler. The volume percent was estimated from the weight loading and densities of PDMS (0.965 g/cm$^3$), silicalite-1 (~1.50 g/cm$^3$), and ZIF-71 (~0.50 g/cm$^3$). Table 6.II below shows the results of this analysis. The 5 wt% (3.27 vol%) silicalite-1($F^-$) film had the greatest improvement on both the ethanol permeability and ethanol/water selectivity, increasing by 5.83 and 1.90 %/vol% loading respectively. This high performance is attributed to both the super-hydrophobicity of the material and the large effective area covered by each crystal associated with the platelet morphology. ZIF-71 had the second largest ethanol permeability increase factor and selectivity increase factors. The significant improvement in both of these factors is due to both the large pore opening of the ZIF-71 structure (0.48 nm) and the very low water uptake of the material (only0.263 mmol/g). While the permeability improvement was

expected, the large selectivity improvement was surprising. Due to the Type-IV ethanol adsorption isotherm, permeability through ZIF-71 was expected to be diffusion control.

**Table 6.II**. Normalized ethanol permeability and ethanol water selectivity for the various mixed matrix membranes.

| Film | Volume loading (%) | % $P_E$ increase/ vol % loading | % α increase/ Vol % loading |
|---|---|---|---|
| 5 wt% Silicalite-1 ($F^-$) | 3.27 | 5.83 | 1.90 |
| 20 wt% Silicalite-1 ($F^-$) | 13.9 | 1.32 | 1.16 |
| 40 wt% Silicalite-1 ($OH^-$) | 30.0 | 0.64 | 0.344 |
| 50 wt% ZIF-71 | 65.9 | 4.36 | 1.04 |

While the 20 wt% (13.9 vol%) silicalite-1($F^-$) film had larger increase factors than the 40 wt% (30.0 vol%) silicalite-1($OH^-$) film, the performance improvement was not as great as was observed for the 5 wt% film. As seen in Figure 3.6 b, the platelets are not as well aligned at the lower loading. It is likely that the twinned nature of the crystals of the sample prevented alignment in the film and thus not taking advantage of the larger effective area.

*Conclusions*

The performance of 4 films (5 wt% silicalite-1($F^-$), 20 wt% silicalite-1($F^-$), 40 wt% silicalite-1($OH^-$), and 50 wt% ZIF-71) at 50ºC with a 3 wt% ethanol feed was determined using pervaperation. Taking into account the filler volume percent in each of the films, the 5 wt% silicalite-1($F^-$) was found to enhance the properties of PDMS the most, improving the permeability of ethanol by 5.83% per vol% loading and increasing the ethanol water selectivity by 1.90% per vol% loading. The super hydrophobicity and large effective area of the platelet crystals largely impacted this performance. If mixed matrix membranes with higher weight loadings of silicalite-1($F^-$) will proper crystal alignment can be achieved, it is likely near zeolite

membrane selectivity can be achieved with advantages of high ethanol flux and the ease of polymer like processability.

Even without having to worry about crystal alignment, both silicalite-1($F^-$) and ZIF-71 offer significant improvement over the more commonly used silicalite-1($OH^-$). For just about any application silicalite-1($OH^-$), silicalite-1($F^-$) and ZIF-71 are better alternatives due largely in part to the super-hydrophobicity of the materials.

## REFERENCES

1. LM Vane, VV Namboodiri, TC Bowen. Hydrophobic zeolite-silicone rubber mixed matrix membranes for ethanol-water separation: Effect of zeolite and silicone component selection on pervaporation performance. *Journal of Membrane Science*, 2008. 308(1-2) p 230 – 241.
2. RP Lively, et al. Chemical Communications. 47 (2011) pp 8667 – 8669.
3. N Bighane and WJ Koros. *Journal of Membrane Scienec*. 371 (2011) pp 254 – 262.